THE STROPHYSICAL JOURNAL, 986:220 25pp), 2025 June 20 https://doi.org/10.3847/1538-4357/add3f5

N-body Simulations of the Self-confinement of Viscous Self-gravitating Narrow Eccentric Planetary Ringlets

Joseph M. Hahn[1], Douglas P. Hamilton[2], Thomas Rimlinger[2], and Yuxi Lucy) Lu[3,4,5]
[1] Space Science Institute, US ; jhahn@spacescience.org
[2] University of Maryland, US
[3] Department of stronomy, The Ohio State University, Columbus, 140 West 18th venue, OH 43210, US
[4] Center for Cosmology and stroparticle Physics CC PP), The Ohio State University, 191 West Woodruff venue, Columbus, OH 43210, US
[5] merican Museum of Natural History, Central Park West, Manhattan, NY 10024, US
Received 2025 March 4; revised 2025 pril 30; accepted 2025 May 1; published 2025 June 19

bstract

Narrow eccentric planetary ringlets have sharp edges, sizable eccentricity gradients, and a confinement mechanism that prevents radial spreading due to ring viscosity. Most proposed ringlet confinement mechanisms presume that there is one or more shepherd satellites whose gravitational perturbations keep the ringlet confined radially, but the absence of such shepherds in Cassini observations of Saturn's rings casts doubt upon those ringlet confinement mechanisms. The following uses a suite of *N*-body simulations to explore an alternate scenario, whereby ringlet self-gravity drives a narrow eccentric ringlet into a self-confining state. These simulations show that, under a wide variety of initial conditions, an eccentric ringlet's secular perturbations of itself causes the eccentricity of its outer edge to grow at the expense of its inner edge. This causes the ringlet's nonlinearity parameter q to grow over time until it exceeds the $q \simeq \sqrt{3}$ 2 threshold where the ringlet's orbit-averaged angular momentum flux due to viscosity + self-gravity is zero. The absence of any net radial angular momentum transfer through the ringlet means that the ringlet has settled into a self-confining state, i.e., it does not spread radially due to its viscosity, and simulations also show that such ringlets have sharp edges. Nonetheless, viscosity still circularizes the ringlet in time $\tau_e \sim 10^6$ orbits ∼1000 yr, which will cause the ringlet's nonlinearity parameter to shrink below the $q \simeq \sqrt{3}$ 2 threshold and allows radial spreading to resume. Either sharp-edged narrow eccentric ringlets are transient phenomena or exterior perturbations are also sustaining the ringlet's eccentricity. We then speculate about how such ringlets might come to be.

Unified stronomy Thesaurus concepts: Planetary rings 1254); Solar system 1528); Saturn 1426); Planetary dynamics 2173); Orbital evolution 1178)

1. Introduction

Narrow eccentric planetary ringlets have properties that are both interesting and not well understood, such as sharp edges, sizable eccentricity gradients, and a confinement mechanism that opposes radial spreading due to ring viscosity. To date, nearly all of the prevailing ringlet confinement mechanisms assume that there also exists a pair of unseen shepherd satellites that straddle the ringlet, and the shepherds' gravities also torque the ringlet's edges in a way that keeps them radially confined P. Goldreich & S. Tremaine 1979a, 1979b, 1981; E. I. Chiang & P. Goldreich 2000; I. Mosqueira & P. R. Estrada 2002). P. Goldreich et al. 1995) show that a single shepherd satellite can provide temporary confinement. However, the local gravitational perturbations exerted by the shepherds on the nearby ring material also excite prominent kinks C. D. Murray et al. 2005) and scalloping J. W. Weiss et al. 2009) of the ring edges, which should invite detection of the hypothetical satellites. That the Cassini spacecraft did not detect any shepherds near Saturn's well-studied narrow ringlets casts doubt upon this ringlet confinement mechanism P. Y. Longaretti 2018).

Note though that N. Borderies et al. 1982) showed that a viscous ringlet having a sufficiently high eccentricity gradient can in fact be self-confining, due to a reversal of its viscous angular momentum flux, which in turn would cause the ringlet to get narrower over time. This suggestion also motivates this study, which uses the epi_int_lite *N*-body integrator to investigate whether a viscous and self-gravitating ringlet might evolve into a self-confining state.

We also note that Uranus hosts several narrow eccentric ringlets, but Section 4.5 uses results from a recent study of the Uranian ringlets R. G. French et al. 2024) to argue that these are not candidates for the self-confinement mechanism that is considered here; see Section 4.5 for details.

2. Epi_int_lite

Epi_int_lite is a child of the epi_int *N*-body integrator that was used to simulate the outer edge of Saturn's B ring while it is sculpted by satellite perturbations J. M. Hahn & J. N. Spitale 2013). The new code is very similar to its parent but differs in two significant ways: i) epi_int_lite is written in Python and is recoded for more efficient execution, and ii) epi_int_lite uses a more reliable drift step to handle unperturbed motion around an oblate planet detailed in ppendix). Otherwise, epi_int_lite's treatment of ring self-gravity and viscosity are identical to that used by the parent code, and see J. M. Hahn & J. N. Spitale 2013) for additional details. The epi_int_lite source code is available on GitHub,[6]

[6] https://github.com/joehahn/epi_int_lite

and the code's numerical quality is benchmarked in ppendix B, where the outputs of several numerical experiments are compared against theoretical expectations.

Calculations by epi_int_lite use natural units with gravitation constant $G = 1$, central primary mass $M = 1$, and the ringlet's inner edge has initial radius $r_0 = 1$, and so the ringlet masses m_r and radii r quoted below are in units of M and r_0. Converting code output from natural units to physical units requires choosing physical values for M and r_0 and multiplying accordingly, and when this text does so it assumes Saturn's mass $M = 5.68 \times 10^{29}$ gm and a characteristic ring radius $r_0 = 1.0 \times 10^{10}$ cm. Simulation time t is in units of $T_{\rm orb}/2\pi$, where $T_{\rm orb} = 2\pi\sqrt{r_0^3\ GM}$ is the orbit period at r_0, so we multiply time t by $T_{\rm orb}/2\pi$ to convert from natural to physical units. The simulated particles' motions during the drift step are also sensitive to the J_2 portion of the primary's nonspherical gravity component see ppendix), and all simulations adopt Saturn-like values of $J_2 = 0.01$ and $R_p = r_0/2$, where R_p is the planet's mean radius.

2.1. Streamlines

Initially, all particles are assigned to various streamlines across the simulated ringlet. streamline is a closed eccentric path around the primary, and each streamline is populated by N_p particles that are initially assigned a common semimajor axis a and eccentricity e while distributed uniformly in longitude. Most of the simulations described below employ only $N_s = 2$ streamlines, so that the model output can be compared against theoretical treatments that also treat the ringlet as two gravitating streamlines e.g., N. Borderies et al. 1983a). But the following also performs a few higher-resolution simulations using $N_s = 3-14$ streamlines, to demonstrate that the $N_s = 2$ treatment is perfectly adequate and reproduces all the relevant dynamics. ll simulations use $N_p = 241$ particles per streamline, and the total number of particles is N_sN_p. Note that the assignment of particles to a given streamline is merely for labeling purposes because particles are still free to wander in response to the ring's internal forces, namely, ring gravity and viscosity. But, as J. M. Hahn & J. N. Spitale 2013) as well as this work shows, the simulated ring stays coherent and highly organized throughout the simulation such that particles on the same streamline do not pass each other longitudinally, nor do they cross adjacent streamlines. Because the simulated ringlet stays highly organized, there is no radial or longitudinal mixing of the ring particles, and simulated particles preserve memory of their streamline membership over time.

The epi_int_lite code also monitors all particles and checks whether any have crossed adjacent streamlines. If this happens, the simulation is then terminated since the particles' subsequent evolution would no longer be computed reliably.

2.2. N-*body Method*

The epi_int_lite N-body integrator uses the same second-order symplectic drift-kick scheme used by the MERCURY N-body algorithm J. E. Chambers 1999), except that epi_int_lite particles do not interact with each other directly. Rather, epi_int_lite particles are only perturbed by the accelerations exerted by the ringlet's individual streamlines. Those accelerations are sensitive to the streamline's relative separations and orientations, which are inferred from the particles' positions and velocities. Epi_int_lite particles are thus tracer particles that indicate the streamlines' locations and orientations, which the N-body integrator uses to compute the orbital evolution of those tracer particles due to the perturbations exerted by those streamlines. This streamline approach is widely used in theoretical studies of planetary rings see P. Goldreich & S. Tremaine 1979a; N. Borderies et al. 1983a, 1985) as well as in N-body studies of rings J. M. Hahn & J. N. Spitale 2013; T. Rimlinger et al. 2016). The great benefit of the streamline concept in numerical work is that it allows one to swiftly track the global evolution of the ringlet's streamlines numerically using only a modest numbers of tracer particles, typically $N_sN_p \sim 500$.

The simulations reported here account for streamline gravity and ringlet viscosity. Because a ringlet is narrow, all particles are in close proximity to the nearby portions of all streamlines, which allows us to approximate a streamline as an infinitely long wire of matter having linear density λ. Consequently, the gravity of each perturbing streamline draws a particle toward that streamline with acceleration

$$_g = \frac{2G\lambda}{\Delta} \quad 1)$$

where Δ is the particle's distance from the streamline.

The streamline's linear density λ is inferred from a streamline's total mass, $m_1 = m_r\ N_s = \int^{2\pi} \lambda d\ell$, where the integration is about the streamline's circumference. Replacing $d\ell$ with vdt where v is the velocity of the streamline's particles allows us to replace the spatial integral with a timewise integral, $m_1 = \int^T \lambda v dt = \lambda v T$, where the streamline's orbital period $T = 2\pi/\Omega$ and Ω its mean orbital frequency, hence

$$\lambda = \frac{m_1\Omega}{2\pi v}. \quad 2)$$

The hydrodynamic approximation is used here to account for the dissipation that occurs as particles in adjacent particle streamlines shear past and collide with the perturbed particle, without having to monitor individual particle–particle collisions. The particle's Eulerian acceleration due to the ring particles' shear viscosity is

$$_{\nu\parallel} = -\frac{1}{\sigma r}\frac{\partial\ _L}{\partial r} \quad 3)$$

where r is the particle's radial coordinate and σ is the surface density

$$\sigma = \frac{\lambda}{\Delta r} \quad 4)$$

where Δr is the radial separation between the particle and the perturbing streamline and see Section 2.3.3 of J. M. Hahn & J. N. Spitale 2013 for details about how that is evaluated numerically), and $_{L\,\nu}$ is the flux of angular momentum that is transported radially across the particle's streamline due to its collisions with particles in adjacent streamlines, i.e.,

$$_{L\,\nu} = -\nu_s\sigma r^2\frac{\partial\omega}{\partial r} \quad 5)$$

where ν_s is the ringlet's kinematic shear viscosity and $\omega = v_\theta/r$ is the particle's angular velocity ppendix of J. M. Hahn & J. N. Spitale 2013). The acceleration $_{\nu,}$ is parallel to the perturbed particle's streamline, i.e., parallel to the particle's

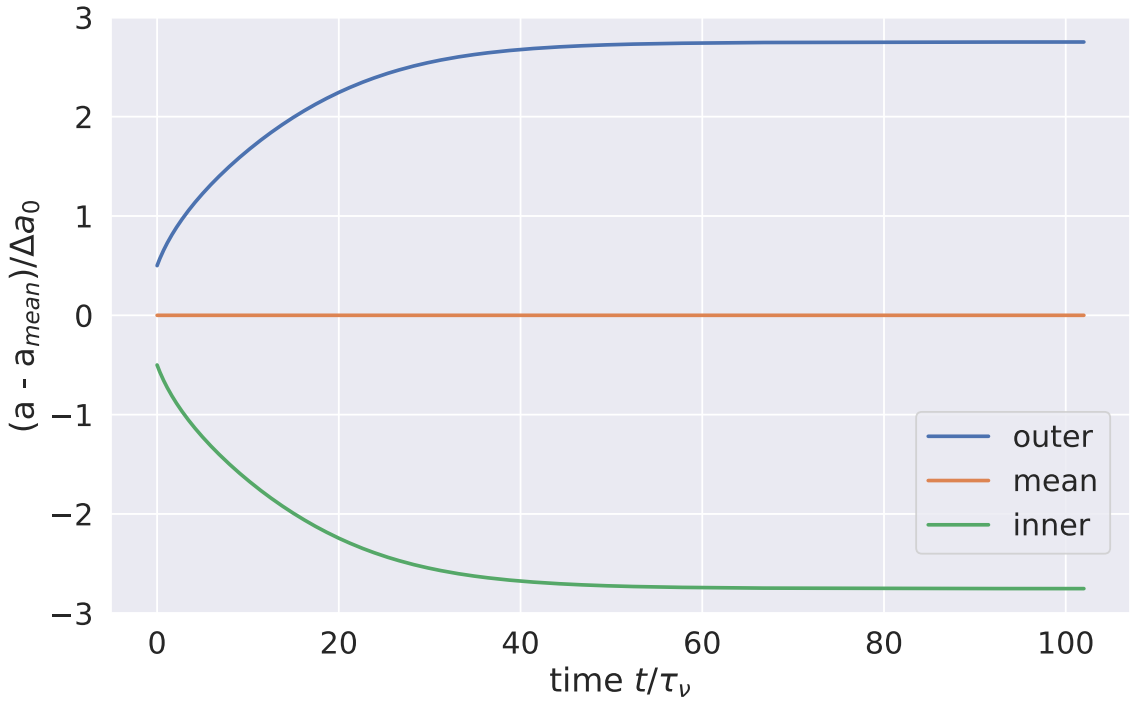

Figure 1. Evolution of the nominal ringlet's semimajor axes a vs. time t in units of the ringlet's viscous timescale $\tau_\nu = 1.3 \times 10^3$ orbital periods. This ringlet is composed of $N_s = 2$ streamlines, and the outer blue) and inner green) streamlines' semimajor axes are plotted relative to their mean $a_{\rm mean}$, and displayed in units of the ringlet's initial width $\Delta a_0 = 10^{-4}$ in natural units i.e., $G = M = r_0 = 1$). The simulated ringlet has total mass $m_r = 10^{-10}$, shear viscosity $\nu_s = 10^{-13}$, and initial eccentricity $e = 0.01$. See Section 3.1 to convert m_r, a, and ν_s from natural units to physical units.

velocity vector $\boldsymbol{v} = \dot{\boldsymbol{r}} = v_r r \quad v_\theta \theta$, where $\boldsymbol{r} = r\boldsymbol{r}$ is the particle's position vector.

Dissipative collisions also transmit linear momentum in the perpendicular direction, which results in the additional acceleration

$$_{\nu\perp} = -\frac{1}{\sigma}\frac{\partial \mathcal{G}}{\partial r} \qquad 6)$$

where the radial flux of linear momentum due to ringlet viscosity is

$$\mathcal{G} = -\left(\frac{4}{3}\nu_s \quad \nu_b\right)\sigma\frac{\partial v_r}{\partial r} - \left(\nu_b - \frac{2}{3}\nu_s\right)\frac{\sigma v_r}{r} \qquad 7)$$

where ν_b is the ringlet's kinematic bulk viscosity, and v_r is the particle's radial velocity J. M. Hahn & J. N. Spitale 2013).

In the hydrodynamic approximation there is also the acceleration due to ringlet pressure p that is due to particle–particle collisions:

$$_{p} = -\frac{1}{\sigma}\frac{\partial p}{\partial r}. \qquad 8)$$

Epi_int_lite treats the particle ring as a dilute gas of colliding particles for which the 1D pressure is $p = c^2\sigma$, where c is the particle's dispersion velocity. However, J. M. Hahn & J. N. Spitale 2013) found ring pressure to be inconsequential in N-body simulations of Saturn's ring, and the ringlet simulation examined in great detail in Section 3.1 also showed no sensitivity to pressure effects, so all other simulations reported on here have $c = 0$.

3. N-body Simulations of Viscous Gravitating Ringlets

The following describes a suite of N-body simulations of narrow viscous gravitating planetary ringlets, to highlight the range of initial ringlet conditions that do evolve into a self-confining state, and those that do not.

3.1. Nominal Model

Figure 1 shows the semimajor axis evolution of what is referred to as the nominal model since this ringlet readily evolves into a self-confining state. The simulated ringlet is composed of $N_s = 2$ streamlines having $N_p = 241$ particles per streamline, and the integrator time step is $\Delta t = 0.5$ in natural units, so the integrator samples the particles' orbits $2\pi/\Delta t \simeq 13$ times per orbit, and this ringlet is evolved for 1.4×10^5 orbits, which requires 50 minutes execution time on a 10 year old laptop. The ringlet's mass is $m_r = 10^{-10}$, its shear viscosity is $\nu_s = 10^{-13}$, and its bulk viscosity is $\nu_b = \nu_s$. The ringlet's initial radial width is $\Delta a_0 = 10^{-4}$, its initial eccentricity is $e = 0.01$, and its eccentricity gradient is initially zero. convenient measure of time is the ringlet's viscous radial spreading timescale,

$$\tau_\nu = \frac{\Delta a_0^2}{12\nu_s} \qquad 9)$$

which can be inferred from Equation 2.13) of J. E. Pringle 1981). This simulation's viscous timescale is $\tau_\nu = 8.3 \times 10^3$ in natural units or $\tau_\nu/2\pi = 1.3 \times 10^3$ orbital periods. If this ringlet were orbiting Saturn at $r_0 = 1.0 \times 10^{10}$ cm, then the simulated ringlet's physical mass would be $m_r = 5.7 \times 10^{19}$ gm, which is equivalent to the mass of a 24 km radius iceball assuming a volume density $\rho = 1$ gm cm^{-3}, and the ringlet's initial physical

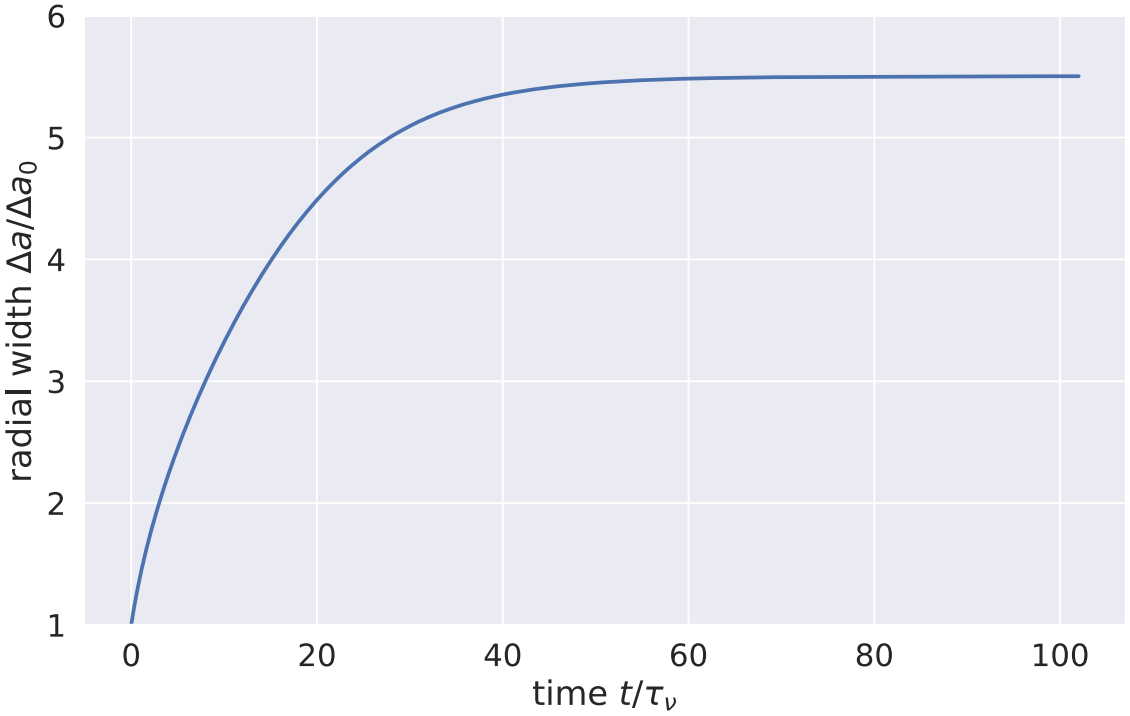

Figure 2. The nominal ringlet's semimajor axis width $\Delta a = a_{\rm outer} - a_{\rm inner}$ over time and in units of its initial radial width Δa_0.

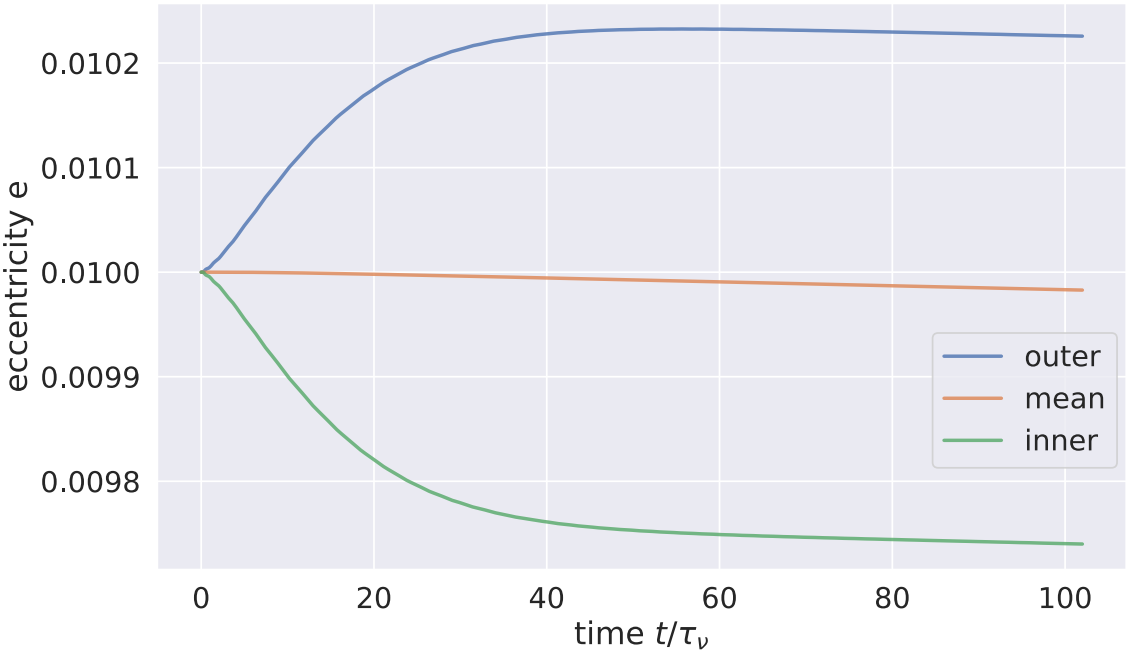

Figure 3. The nominal ringlet's eccentricity evolution.

radial width would be $\Delta a_0 = 10^{-4} r_0 = 10\,\mathrm{km}$. This ringlet's orbit period would be $T_{\rm orb} = 2\pi\sqrt{r_0^3\ GM} = 9.0\,\mathrm{hr}$ in physical units, so the ringlet's viscous timescale is $\tau_\nu = 1.4\,\mathrm{yr}$, and so its shear viscosity is $\nu_s \quad \Delta a_0^2\ 12\tau_\nu \quad 1.9 \times 10^3\,\mathrm{cm^2\,s^{-1}}$ when evaluated in physical units. This ringlet's initial surface density would be $\sigma = m_r/2\pi r_0 \Delta a_0 = 900\,\mathrm{gm\,cm^{-2}}$, but Figures 1–2 show that it shrinks by a factor of about 5 as the ringlet's semimajor axis width Δa grows via viscous spreading until it settles into the self-confining state at time $t \sim 40\tau_\nu$. This so-called nominal ringlet is probably somewhat overdense and overly viscous compared to known planetary ringlets, but that is by design so that the simulated ringlet quickly settles into the self-confining state. Section 4.5 also shows how outcomes vary when a wide variety of alternate initial masses, widths, and viscosities are also considered.

Figure 3 shows that the outer streamline's eccentricity initially grows at the expense of the inner streamline's, and that is a consequence the self-gravitating ringlet's secular perturbations of itself, which is also demonstrated in ppendix C. Figure 4 shows the ringlet's eccentricity difference

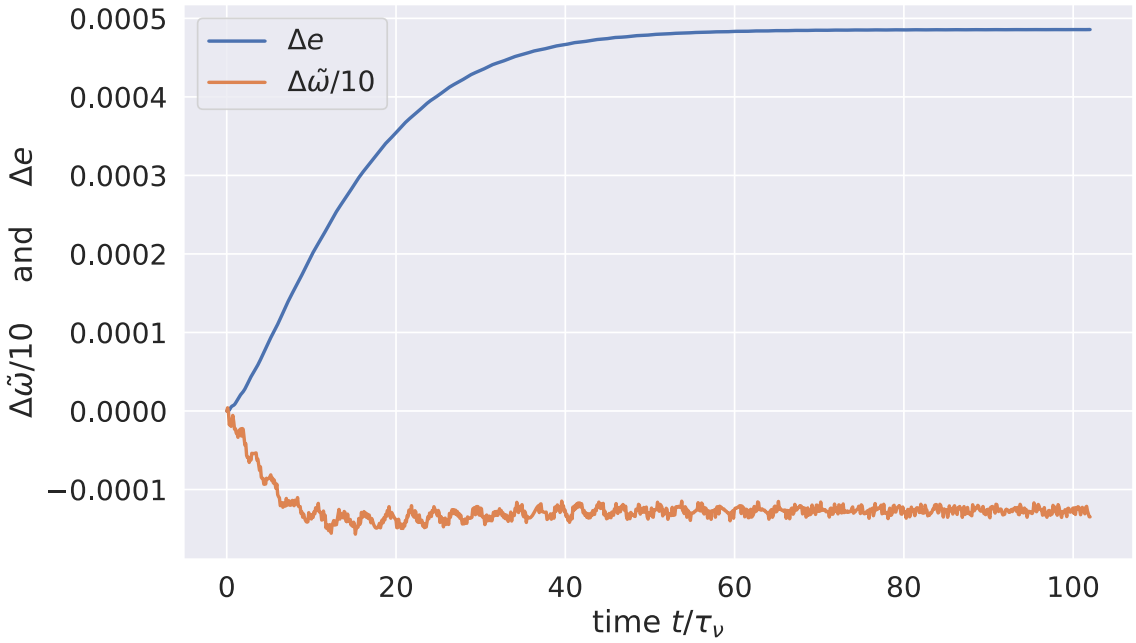

Figure 4. The nominal ringlet's eccentricity difference $\Delta e = e_{\rm outer} - e_{\rm inner}$ and longitude of periapse difference $\Delta\tilde{\omega} = \tilde{\omega}_{\rm outer} - \tilde{\omega}_{\rm inner}$ in radians divided by 10.

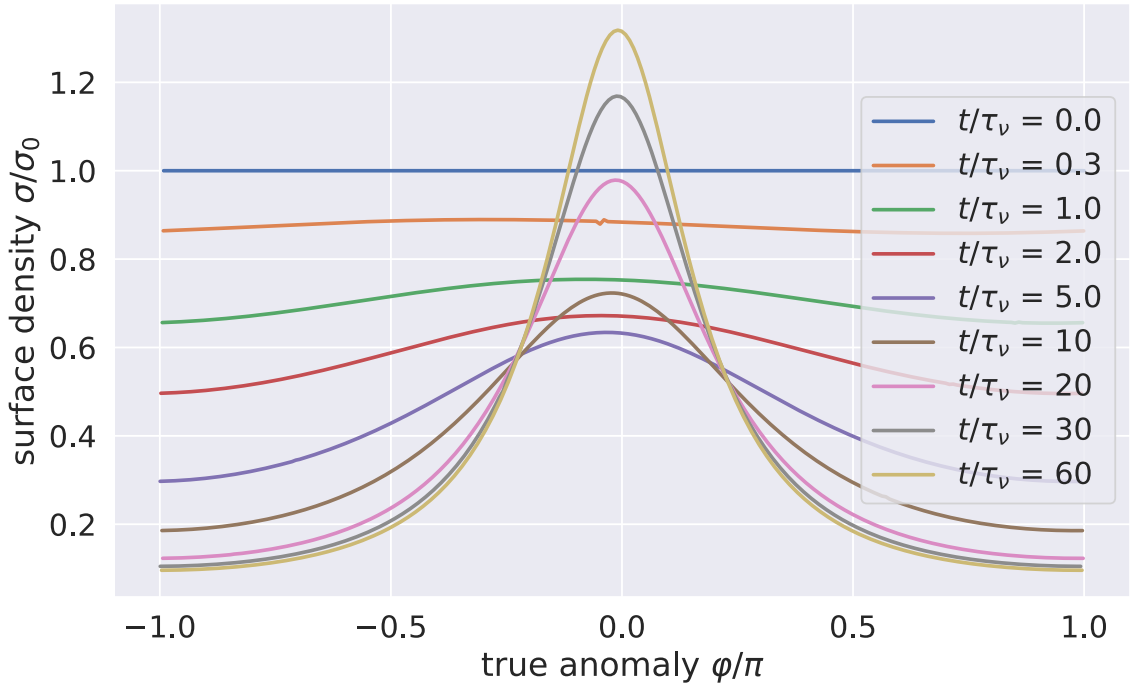

Figure 5. Nominal ringlet's surface density σ φ) vs. true anomaly φ at selected times t and plotted in units of ringlet's initial mean surface density σ_0. Note that the ringlet's surface density maxima occurs just before periapse, and is due to the ringlet's negative periapse twist $\Delta\tilde{\omega} = \tilde{\omega}_{\rm outer} - \tilde{\omega}_{\rm inner} < 0$.

$\Delta e = e_{\rm outer} - e_{\rm inner}$ and longitude of periapse difference $\Delta\tilde{\omega} = \tilde{\omega}_{\rm outer} - \tilde{\omega}_{\rm inner}$, which both settle into equilibrium values after the ringlet arrives at the self-confining state.

In all of the self-confining ringlet simulations examined here, the ringlet's periapse twist $\Delta\tilde{\omega} = \tilde{\omega}_{\rm outer} - \tilde{\omega}_{\rm inner}$ is negative, so the outer streamline's longitude of periapse $\tilde{\omega}$ trails the inner streamline's, which in turn causes the streamlines' separations along the ringlet's preperiapse side where $\varphi = \theta - \tilde{\omega} <$) to differ slightly from the postperiapse $\varphi > 0$) side. Which in turn makes the ringlet's surface density asymmetric, i.e., is maximal just prior to periapse; see Figures 5–6.

It is convenient to recast these orbit element differences as dimensionless gradients,

$$e' = a\frac{de}{da} \quad \text{and} \quad \tilde{\omega}' = ea\frac{d\tilde{\omega}}{da} \qquad 10)$$

because these are the terms that contribute to the nonlinearity parameter of N. Borderies et al. 1983a):

$$q = \sqrt{e'^2 \quad \tilde{\omega}'^2}. \qquad 11)$$

See also Figure 7, which plots the nominal ringlet's dimensionless eccentricity gradient e', dimensionless periapse

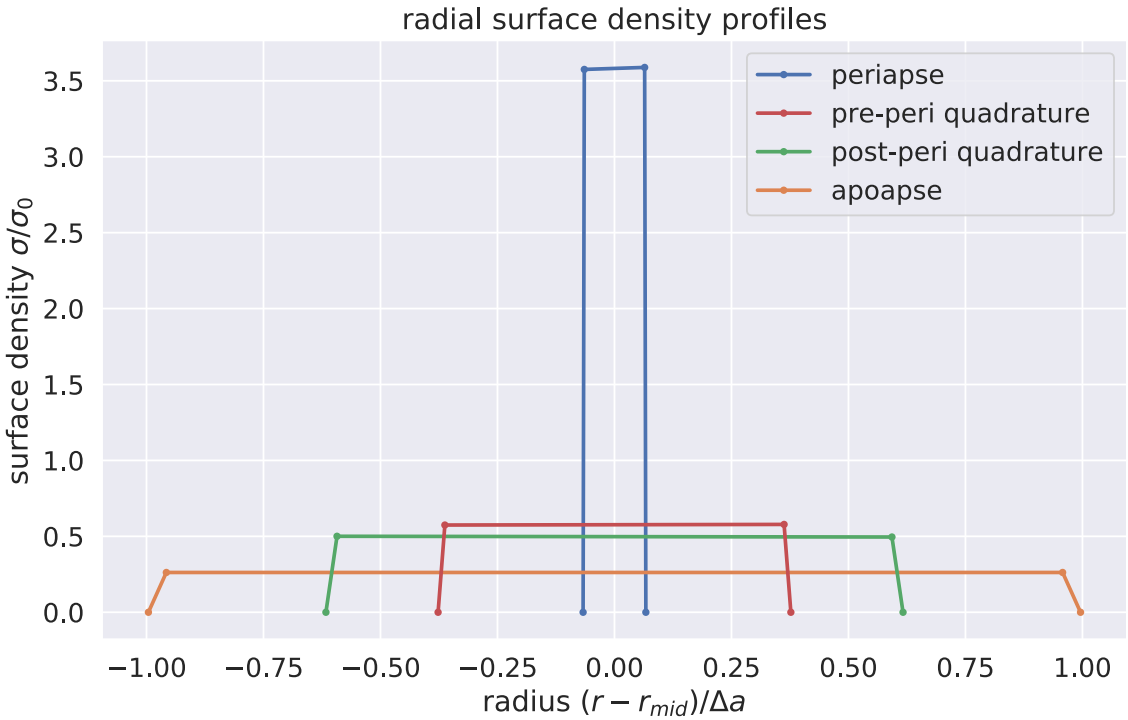

Figure 6. Radial profiles of the nominal ringlet's surface density σ φ) at time $t = 100\tau_\nu$ when the ringlet is self-confining. Each surface density profile is plotted vs. radial distance r relative to $r_{\rm mid}$, which is the ringlet's midpoint along true anomaly $\varphi = \theta - \tilde{\omega}$, with those radial distances $r - r_{\rm mid}$ measured in units of the ringlet's final semimajor axis width Δa, and surface density is shown in units of the ringlet's longitudinally averaged surface density σ_0. Radial surface density profiles are plotted along the ringlet's periapse $\varphi = 0$, blue curve), which is where the ringlet's streamlines are most concentrated and surface density σ is greatest due to the ringlet's eccentricity gradient e', at the preperiapse quadrature $\varphi = -\pi/2$, red curve), postperiapse quadrature $\varphi = \pi/2$, green curve), and at apoapse $|\varphi| = \pi$, orange curve) where streamlines have their greatest separation and ringlet surface density is lowest. This ringlet's surface density contrast between periapse and apoapse is about 14.

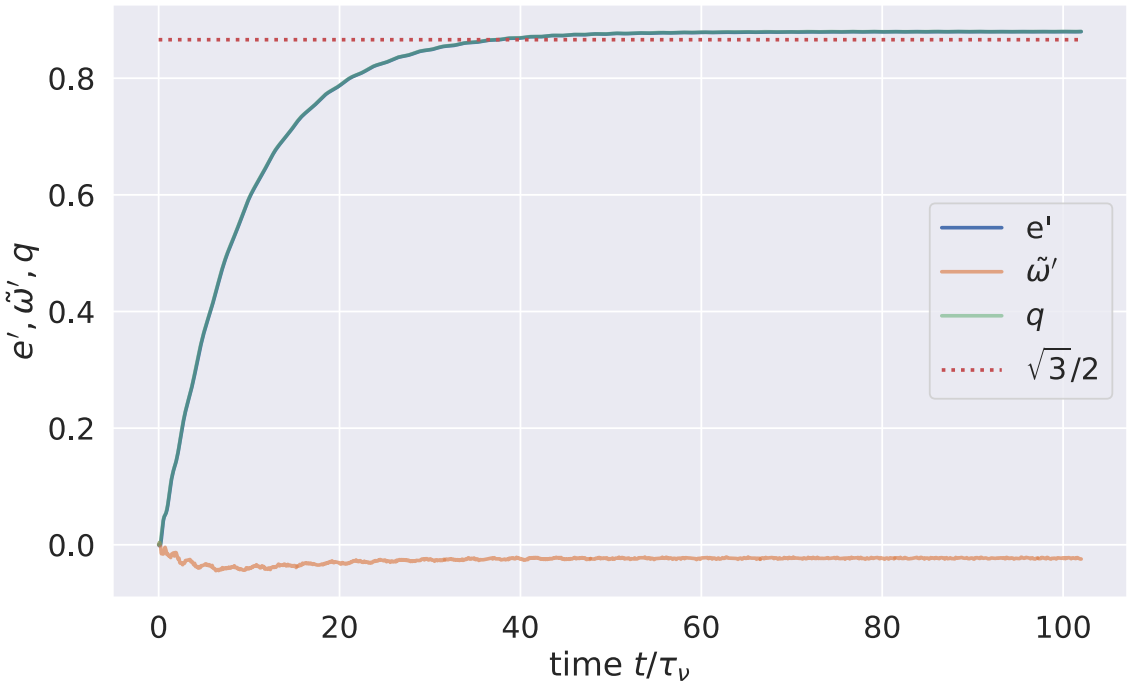

Figure 7. The nominal ringlet's dimensionless eccentricity gradient $e' = a\Delta e$ Δa blue curve), dimensionless periapse twist $\tilde{\omega}' = ea\Delta\tilde{\omega}$ Δa orange), and nonlinearity parameter $q = \sqrt{e'^2 \quad \tilde{\omega}'^2}$ green curve which overlaps blue) vs. time t/τ_ν. Dotted red line is the threshold for self-confinement in a nongravitating ringlet, $e' = \sqrt{3}$ 2 $\simeq 0.866$

twist $\tilde{\omega}'$, and nonlinearity parameter q versus time. ll simulated self-confining ringlets have a positive eccentricity gradient and a negative periapse twist, such that the outer ringlet's periapse trails the inner ringlet's, consistent with the findings of N. Borderies et al. 1983a).

4. ngular Momentum and Energy Fluxes and Luminosities

The nominal ringlet's evolution is readily understood when the ringlet's radial flux of angular momentum and energy are considered.

4.1. ngular Momentum and Energy Fluxes

The torque that is exerted on a small streamline segment of mass δm at location $\boldsymbol{r} = r\boldsymbol{r}$ due to the streamlines orbiting interior to it is $\delta T = \delta m \boldsymbol{r} \times {}^{1}$, where $= {}_{r}\boldsymbol{r}$ ${}_{\theta}\boldsymbol{\theta}$ is the so-called one-sided acceleration that is exerted on δm by all other streamlines interior to it. Since $\delta m = \lambda \delta \ell$, where λ is the streamline's linear mass density and $\delta \ell$ is the segment's length, then the radial flux of angular momentum flowing into that segment due to the accelerations that are exerted by streamlines interior to that segment is

$$ {}_{L}\, r\ \theta) = \frac{\delta T}{\delta \ell} = \lambda r\ {}^{1}_{\theta} \tag{12} $$

where ${}_{\theta}$ is the tangential component of the one-sided acceleration and the streamline's linear mass density λ is computed using Equation 2). The radial angular momentum flux, Equation 12), is due to the ringlet's viscosity and self-gravity, so ${}_{L} =$ ${}_{L\,\nu}$ ${}_{L\,g}$, where

$$ {}_{L\,\nu} = \lambda r\ {}^{1}_{\nu\,\theta} \tag{13} $$

and

$$ {}_{L\,g} = \lambda r\ {}^{1}_{g\,\theta} \tag{14} $$

are the viscous and gravitational angular momentum fluxes at a particle. The particle's one-sided gravitational acceleration ${}^{1}_{g\,\theta}$ is straightforward to compute, it is merely the tangential component of the gravitational accelerations exerted by all streamlines orbiting interior to the particle, while the viscous angular momentum flux is Equation 5) derived in J. M. Hahn & J. N. Spitale 2013).

The work that the interior streamlines exert on δm as that segment travels a small distance $\delta \boldsymbol{r} = \boldsymbol{v}\delta t$ in time δt is $\delta W = \delta m\ {}^{1} \cdot \delta \boldsymbol{r}$, where $\boldsymbol{v} = v_r \boldsymbol{r}$ $v_\theta \boldsymbol{\theta}$ is the segment's velocity, and that work accrues at δm at the rate $\delta W/\delta t = \lambda\ {}^{1} \cdot \boldsymbol{v}\delta \ell$, so the radial flux of energy entering that ringlet segment due to accelerations exerted by the interior streamlines is

$$ {}_{E}\, r\ \theta) = \frac{\delta W}{\delta \ell \delta t} = \lambda\ {}^{1} \cdot \boldsymbol{v}. \tag{15} $$

The radial energy flux is due to the ringlet's viscosity and self-gravity, so ${}_{E} =$ ${}_{E\,\nu}$ ${}_{E\,g}$.

4.2. Luminosities

The streamline-containing segment δm has semimajor axis a, and integrating the radial angular momentum flux ${}_{L}$ about the entire streamline then yields the radial luminosity of angular momentum entering streamline a,

$$ \mathcal{L}_{L}\ a) = \oint\ {}_{L} d\ell \tag{16} $$

which is the torque that is exerted on streamline a by those orbiting interior to it. Similarly, integrating the radial energy flux ${}_{E}$ about streamline a also yields the ringlet's radial energy luminosity

$$ \mathcal{L}_{E}\ a) = \oint\ {}_{E} d\ell \tag{17} $$

which is the rate that the interior streamlines communicate energy to streamline a.

4.3. Viscous Transport of ngular Momentum

ngular momentum is transported radially through the ring via viscosity and self-gravity, so ${}_{L} =$ ${}_{L\,\nu}$ ${}_{L\,g}$, where the ringlet's viscous flux of angular momentum is

$$ {}_{L\,\nu}\ r\ \theta) = -\nu_s \sigma r^2 \frac{\partial \omega}{\partial r} \tag{18} $$

when Equation 5) is written as a function of spatial coordinates and angular velocity $\omega = \dot{\theta}$. The ring's surface density σ is Equation 4), where $\Delta r \simeq \Delta a\ 1 - e^{'} \cos \varphi)$ when it is assumed that the ringlet's eccentricity e is small but its eccentricity gradient $e^{'} = a \partial e\ \partial a$ might not be, so

$$ \sigma \simeq \frac{\sigma_0}{1 - e^{'} \cos \varphi} \tag{19} $$

where $\sigma_0 = \lambda/\Delta a$ would be the ringlet's initial surface density assuming its initial $e^{'}$ was zero and $\varphi = \theta - \tilde{\omega}$ is the true anomaly, i.e., the longitude relative to periapse. Now consider a small arc of ring material of length $d\ell$, so ${}_{L\,\nu} d\ell$ is the torque that arc exert exerts on ring matter just exterior due to viscous friction, and is the rate that friction transmits angular momentum radially across that arc. nd when ${}_{L\,\nu}$ is evaluated along a single eccentric streamline of semimajor axis a, the above simplifies to

$$ {}_{L\,\nu}\ a\ \varphi) = {}_{L\,\nu\,c} \frac{1 - \frac{4}{3} e^{'} \cos \varphi}{1 - e^{'} \cos \varphi)^2} \tag{20} $$

where the angular shear $\omega^{'} = \partial \omega\ \partial r$ in Equation 18) is derived in ppendix , Equation 11), and ${}_{L\,\nu\,c} = \frac{3}{2} \nu_s \sigma_0 a \Omega$ is the viscous angular momentum flux through a circular streamline of semimajor axis a that has angular speed $\Omega\ a)$. Note that Equation 20) is equivalent to Equation 18) of N. Borderies et al. 1982) provided $|\tilde{\omega}'| \ll e^{'}$ such that $q \simeq e^{'}$.

Integrating the above around the streamline's circumference then yields its angular momentum luminosity,

$$ \mathcal{L}_{L\,\nu}\ a) = \oint\ {}_{L\,\nu}\ a\ \varphi) r d\varphi = \mathcal{L}_{L\,\nu\,c} \frac{1 - \frac{4}{3} e^{'2}}{1 - e^{'2})^{3\ 2}} \tag{21} $$

which is the torque that one streamline exerts on its exterior neighbor due to viscous friction N. Borderies et al. 1982) with $\mathcal{L}_{L\,\nu\,c} = 3\pi \nu_s \sigma_0 a^2 \Omega$ being the viscous angular momentum luminosity of a circular streamline.

N. Borderies et al. 1982) examine angular momentum transport through a viscous eccentric but nongravitating

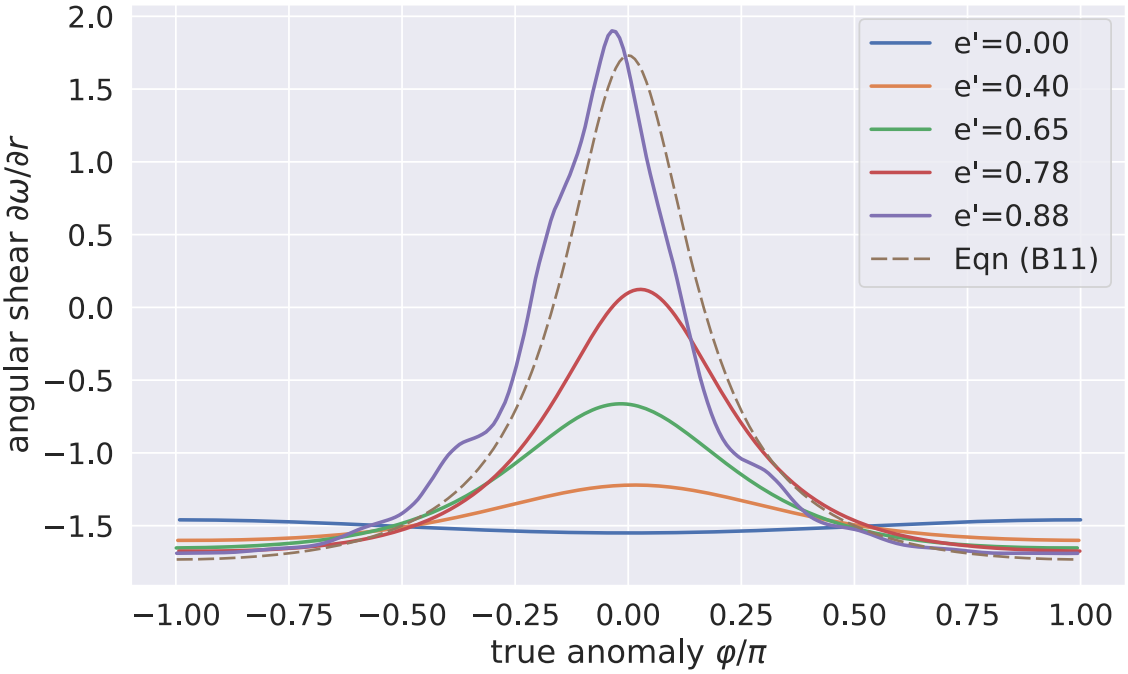

Figure 8. The nominal ringlet's angular shear $\partial\omega/\partial r$ is plotted vs. true anomaly φ at selected moments in time; this quantity is negative where the inner streamline has the higher angular speed $\omega = \nu_\theta/r$. When the simulation starts, the ringlet has eccentricity $e = 0.01$ and eccentricity gradient $e' =$ so $\partial\omega/\partial r \simeq -3\Omega/2r \simeq -1.5$ when evaluated natural units blue curve). The ringlet's e' then grows over time orange, green, and red curves), which reverses the sign of $\partial\omega/\partial r$ near periapse when $e' > 0.75$; here the inner ringlet's angular speed is slower than the outer ringlet, and viscous friction causes angular momentum to instead flow inwards at these longitudes. The dashed curve is Equation 11) with $e' = \sqrt{3}$ 2 and assuming $|\tilde{\omega}'| \ll 1$.

ringlet, and use Equations 20) and 21) to show that this transport has three regimes distinguished by the ringlet's e':

1. $e' < 3$ 4. The ringlet's viscous angular momentum flux $_{L\nu}\varphi) > 0$ at all longitudes φ. The ringlet's viscous angular momentum luminosity $\mathcal{L}_{L\nu} > 0$, so viscous friction transports angular momentum radially outwards, and the inner ring matter evolves to smaller orbits while exterior ring matter evolves outwards, and the ringlet spreads radially.
2. 3 4 $\leqslant e' < \sqrt{3}$. In this regime there is a range of longitudes φ where the viscous angular momentum flux is reversed such that $_{L\nu}\varphi) < 0$. This angular momentum flux reversal is due to the $\partial\omega/\partial r$ term in Equation 5) changing sign near periapse when $e' > 0.75$; see Figure 8. Nonetheless $\mathcal{L}_{L\nu}$, which is proportional to the orbit-average of $_{L\nu}\varphi)$, is positive and the ringlet still spreads radially, albeit slower than when $e' < 0.75$.
3. $e' \geqslant \sqrt{3}$. Viscous angular momentum flux reversal is complete such that $\mathcal{L}_{L\nu} \leqslant 0$, viscous friction transports angular momentum radially inwards, and the ringlet shrinks radially. But if $e' = \sqrt{3}$ 2 $\simeq 0.866$, then $\mathcal{L}_{L\nu} = 0$ and the ringlet's radial evolution ceases, and the viscous but nongravitating ringlet is self-confining.

Note though that the nominal ringlet's eccentricity gradient exceeds the $e' = \sqrt{3}$ 2 $\simeq 0.866$ threshold dotted red line in Figure 7) when it settles into self-confinement. This is due to the ringlet's self-gravity, which also transports a flux of angular momentum $_{Lg}$ radially through the ringlet.

Figure 9 shows the nominal ringlet's viscous angular momentum flux $_{L\nu}$ versus true anomaly $\varphi = \theta - \tilde{\omega}$ at selected times t. Early in the ringlet's evolution when time $t \leqslant 10\tau_\nu$ blue, orange, green, red, purple, and brown curves), the ringlet is in regime 1 since $e' < 0.75$ and $_{L\nu}\varphi) > 0$ at all longitudes. But by time $t \geqslant 20\tau_\nu$ pink curve), this ringlet's eccentricity gradient exceeds 0.75 and angular momentum flux reversal $_{L\nu}\varphi) < 0$ occurs near periapse where $|\varphi| \simeq 0$, where the ringlet is most overdense due to its eccentricity gradient; see also Figure 6. This ringlet is now in regime 2 and its radial spreading is reduced by angular momentum flux reversal. nd by time $t = 60\tau_\nu$ yellow curve), this ringlet is seemingly in regime 3 since $e' > 0.866$, so one might expect the ringlet to start contracting now, but keep in mind that the above analysis ignores any transport of angular momentum via ringlet self-gravity. Figure 2 in fact shows that this gravitating ringlet's spreading had ceased by time $t \simeq 80\tau_\nu$, at which point $e' = 0.88$ Figure 9 yellow curve), angular momentum flux reversal is nearly complete, and the ringlet's total angular momentum luminosity $\mathcal{L}_L = \mathcal{L}_{L\nu}$ $\mathcal{L}_{Lg}$ is very close to zero. Figures 10 and 11 also show that when the ringlet is self-confining at times $t \geqslant 80\tau_\nu$, its small but positive viscous angular momentum luminosity $\mathcal{L}_{L\nu} \simeq 0.006\mathcal{L}_{L\nu c}$ is counterbalanced by its negative gravitational angular momentum luminosity $\mathcal{L}_{Lg} \simeq -0.006\mathcal{L}_{L\nu c}$, so radial spreading has ceased and the ringlet is self-confining.

4.4. Gravitational Transport

The nominal ringlet's viscous $_{L\nu}$ and gravitational $_{Lg}$ angular momentum fluxes are shown Figure 12 after it has settled into the self-confining state. This figure shows how viscous friction tends to transport angular momentum radially inwards, $_{L\nu}\varphi) < 0$, at longitudes nearer periapse where $|\varphi| \sim 0$, and outwards at all other longitudes, with that flux reversal being due to the reversal of the ringlet's angular

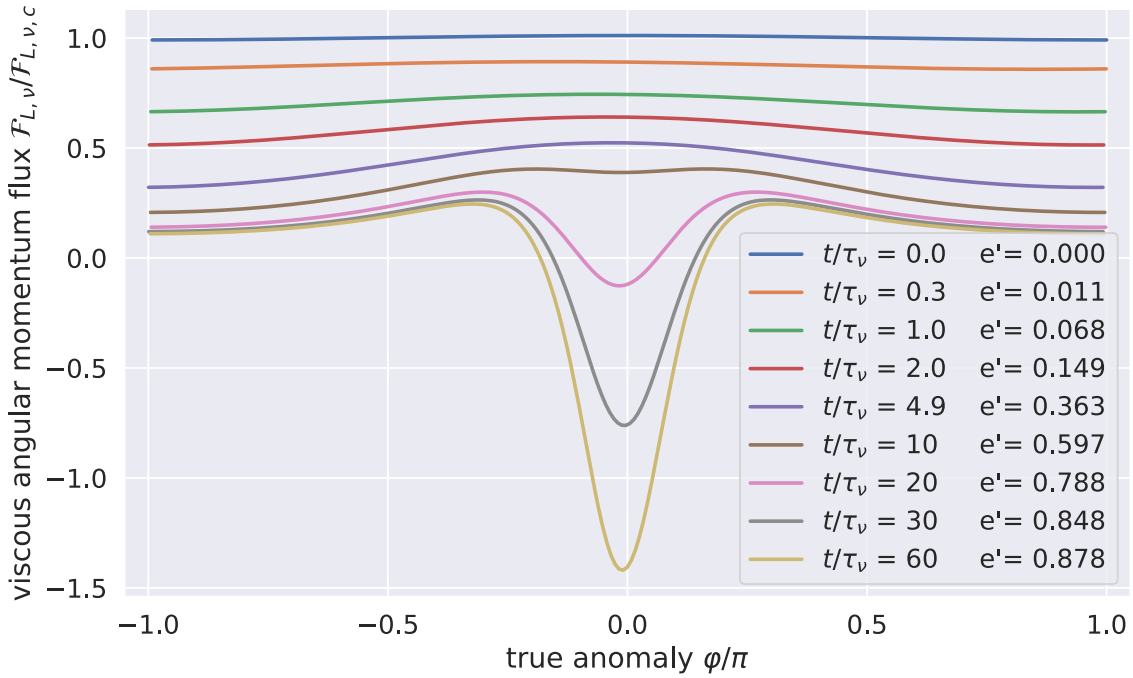

Figure 9. The nominal ringlet's viscous angular momentum flux $_{L\nu}\varphi$), Equation 20), is plotted in units of $_{L\nu c}$ the angular momentum flux in a circular ringlet) and vs. the ringlet's true anomaly $\varphi = \theta - \tilde{\omega}$ at selected times t/τ_ν, with the ringlet's eccentricity gradient e' also indicated.

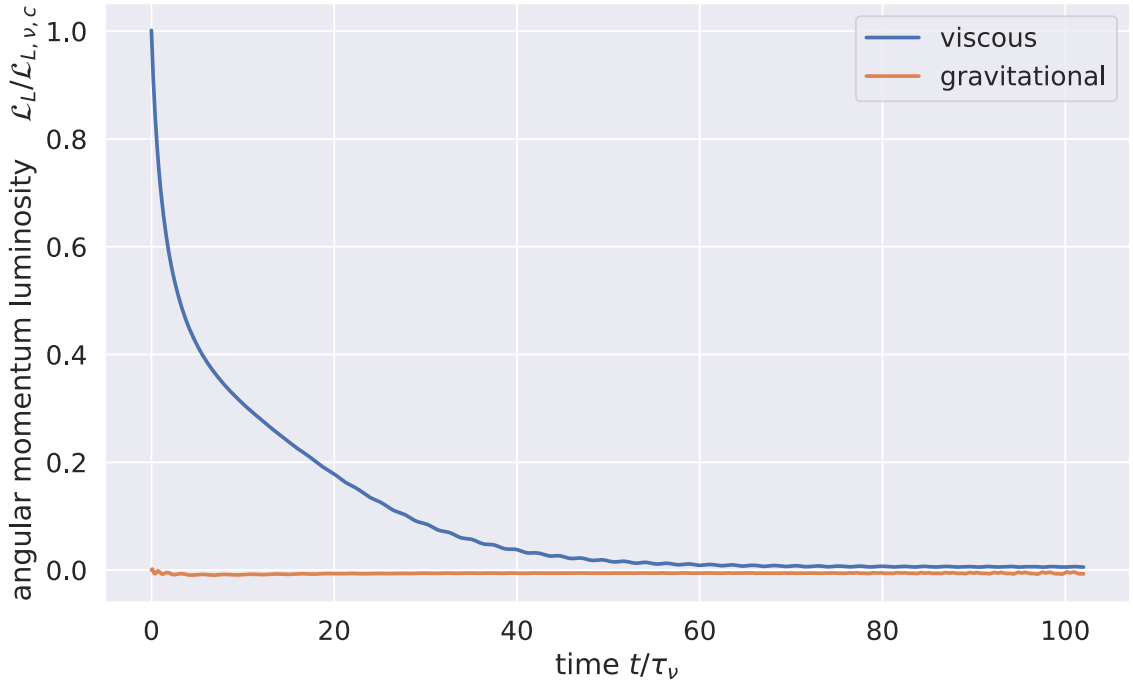

Figure 10. Nominal ringlet's viscous angular momentum luminosity $\mathcal{L}_{L\nu}$ blue curve) vs. time t/τ_ν and in units of a circular ring's viscous angular momentum luminosity $\mathcal{L}_{L\nu c}$, as well as the ringlet gravitational angular momentum luminosity $\mathcal{L}_{Lg}$ orange curve).

velocity gradient; see Figure 8. Figure 12 also shows that the ringlet's gravitational transport of angular momentum is inwards as ring matter approaches periapse where $\varphi < 0$, and is outwards $_{Lg}\varphi) > 0$ postperiapse, with that asymmetry being due to the ringlet's negative periapse twist, $\tilde{\omega}' <$ Figure 7). See also ppendix B, which derives the ringlet's gravitational angular momentum flux $_{Lg}\varphi)$ as a function of its eccentricity gradient e'.

Figure 13 shows the ringlet's energy fluxes due to viscosity blue curve) and gravity orange) at simulation end. Integrating these fluxes about a streamline's circumference at various times t then yields the the ringlet's viscous $\mathcal{L}_{E\nu}$ and gravitational energy luminosity $\mathcal{L}_{Eg}$ over time see Figure 14), where the gravitational energy luminosity is computed via

$$\mathcal{L}_{g}a) = \oint {}_{g}\varphi) r d\varphi = \oint \lambda r \,{}^{1}_{g} \cdot \boldsymbol{v} d\varphi \qquad 22)$$

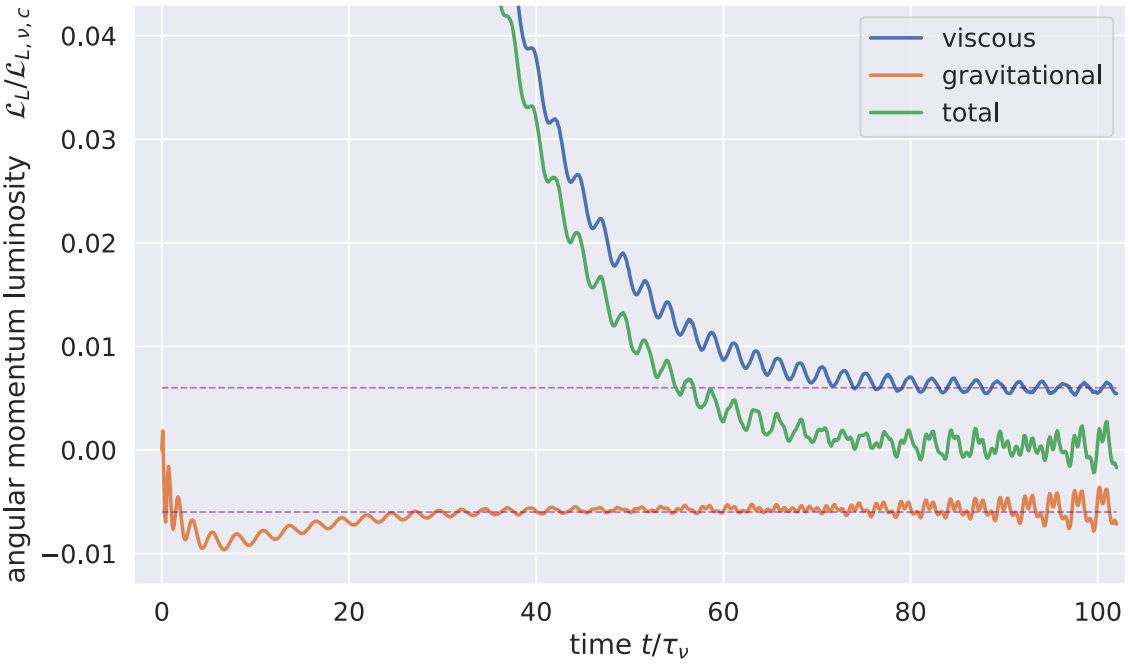

Figure 11. Figure 10 is replotted to show that the ringlet's viscous angular momentum luminosity $\mathcal{L}_{L\,\nu}$ blue curve) always stays positive indicating that the viscous transport of angular momentum is radially outwards) and is eventually balanced by the ringlet's negative i.e., inwards) gravitational angular momentum luminosity $\mathcal{L}_{L\,g}$ orange) after time $t \geqslant 80\tau_\nu$. The green curve is total angular momentum luminosity $\mathcal{L}_{L\,\nu}$ $\mathcal{L}_{L\,g}$, whose time-average is zero when $t \geqslant 80\tau_\nu$. Dashed lines are $\pm 0.006\mathcal{L}_{L\,\nu\,c}$.

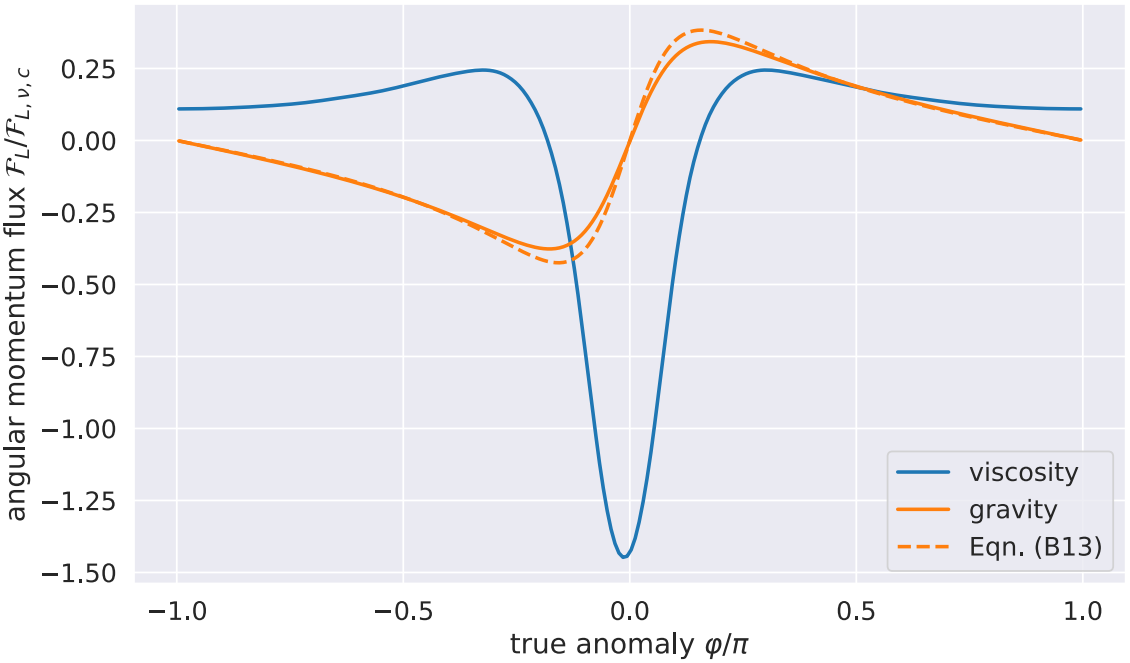

Figure 12. The nominal ringlet's viscous angular momentum flux $_{L\,\nu}\,\varphi)$ blue curve) is computed via Equation 5) and plotted in units of a circular ringlet's flux $_{L\,\nu\,c}$ vs. true anomaly φ at the simulation's end time $t = 100\tau_\nu$, as well as the ringlet's gravitational angular momentum flux $_{L\,g}\,\varphi)$ orange curve) computed via Equations 1) and 14). The dashed curve shows that the approximate gravitational flux, Equation B2), which is derived in ppendix B, agrees very well with the exact flux solid curve) that is derived from this simulation.

where $^{1}_{g}$ is the one-sided gravitational acceleration experienced by a particle in streamline a. Note that even though $_{E\,\nu}$ and $_{E\,g}$ have very different spatial dependences see Figure 13), the influence of the ringlet's viscosity and gravity still conspire such that their orbit-integrated luminosities $\mathcal{L} = \oint\ _{\nu}\ _{g})rd\varphi$ are zero once the ringlet has settled into the self-confining state.

Figure 14 also shows that the ringlet's gravitational energy luminosity is zero at all times. Which is to be expected since the streamlines' gravitating ellipses only interact via their

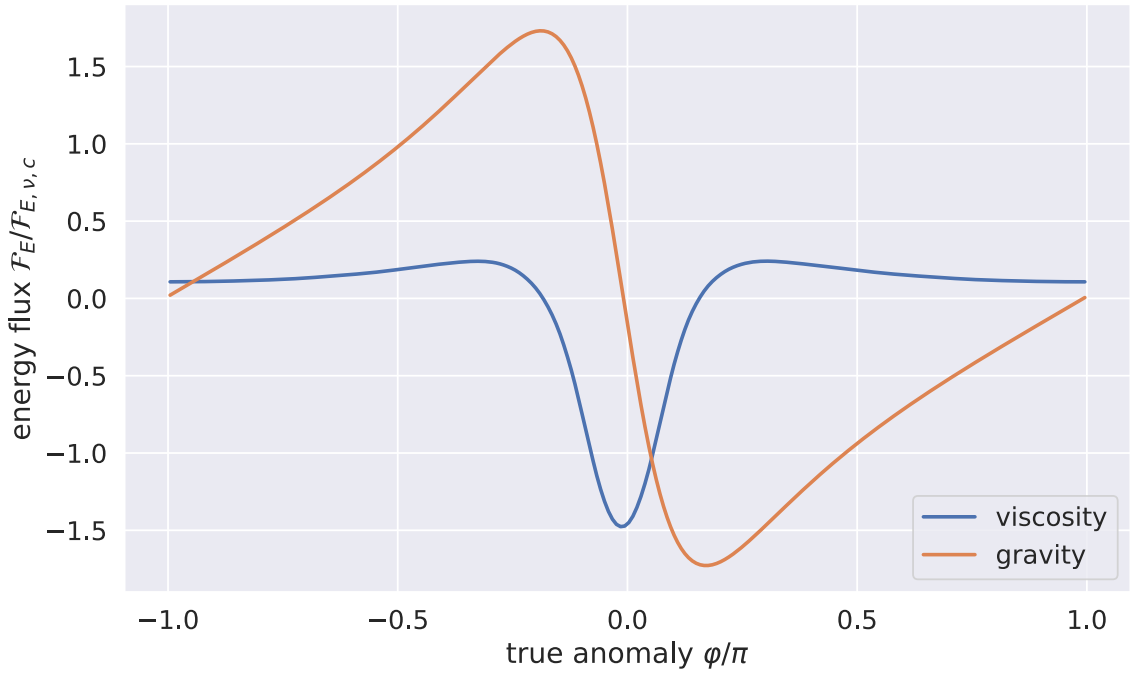

Figure 13. The blue curve is the nominal ringlet's viscous energy flux $_{E\,\nu}\,\varphi$), plotted in units of a circular ringlet's viscous energy flux $_{E\,\nu\,c}$ and vs. the ringlet's true anomaly φ at the simulation's end time $t = 100\tau_\nu$, as well as the ringlet's gravitational energy flux $_{E\,g}\,\varphi$).

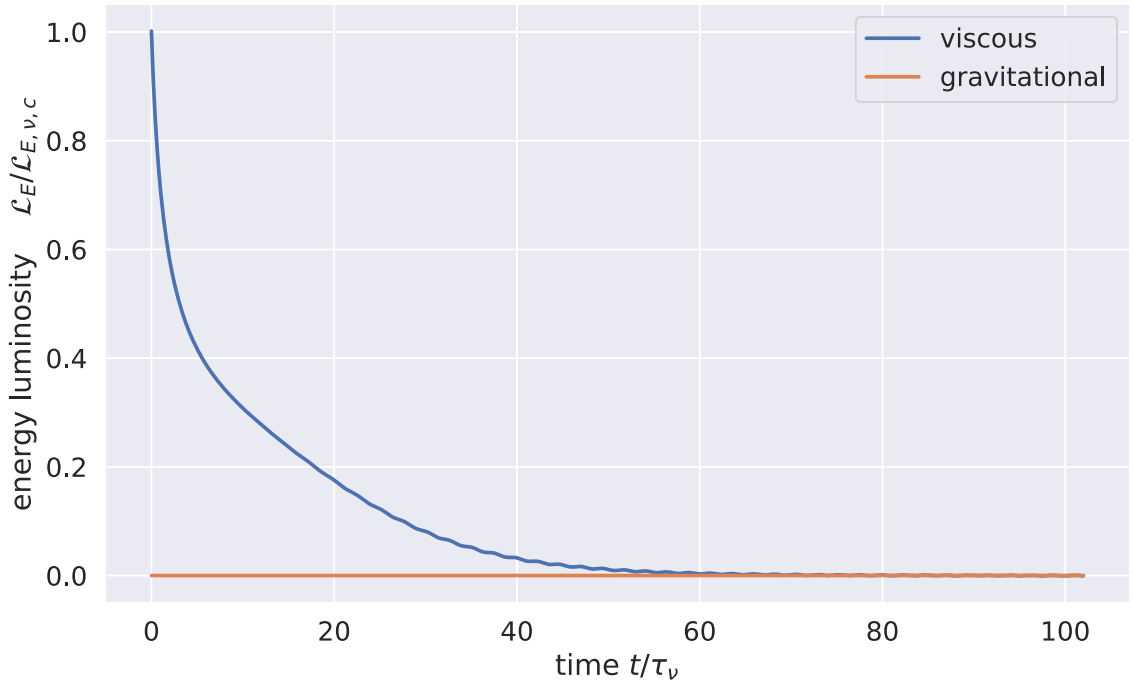

Figure 14. Nominal ringlet's viscous energy luminosity $\mathcal{L}_{E\,\nu}$ blue curve) vs. time t/τ_ν and in units of a circular ring's viscous energy luminosity $\mathcal{L}_{E\,\nu\,c}$, as well as the ringlet gravitational energy luminosity $\mathcal{L}_{E\,g}$ orange curve).

secular perturbations, and secular perturbations do not work D. Brouwer & G. M. Clemence 1961), hence $\mathcal{L}_{E\,g} = 0$. That this quantity evaluates to zero within $\pm 5 \times 10^{-24}$ in natural units) can also be regarded as another test of the epi_int_lite integrator's numerical quality.

4.5. Variations with Ringlet Width, Mass, and Viscosity

To assess whether the nominal ringlet's evolution is typical of other ringlets having alternate values of initial width Δa, total mass m_r, and shear viscosity ν_s, a survey of 571 additional ringlet simulations is executed. These survey ringlets are similar to the nominal ringlet with $N_s = 2$ streamlines having $N_p = 241$ particles per streamline, initial eccentricity $e = 0.01$, initial eccentricity gradient $e' =$, and viscosities $\nu_b = \nu_s$. But the survey ringlets instead have total masses that are geometrically distributed between $10^{-14} \leqslant m_r \leqslant 10^{-9}$, shear viscosities distributed between $10^{-15} \leqslant \nu_s \leqslant 10^{-11}$, and initial radial widths distributed between $2.5 \times 10^{-5} \leqslant \Delta a \leqslant 2.0 \times 10^{-4}$. Survey results are summarized in Figure 15,

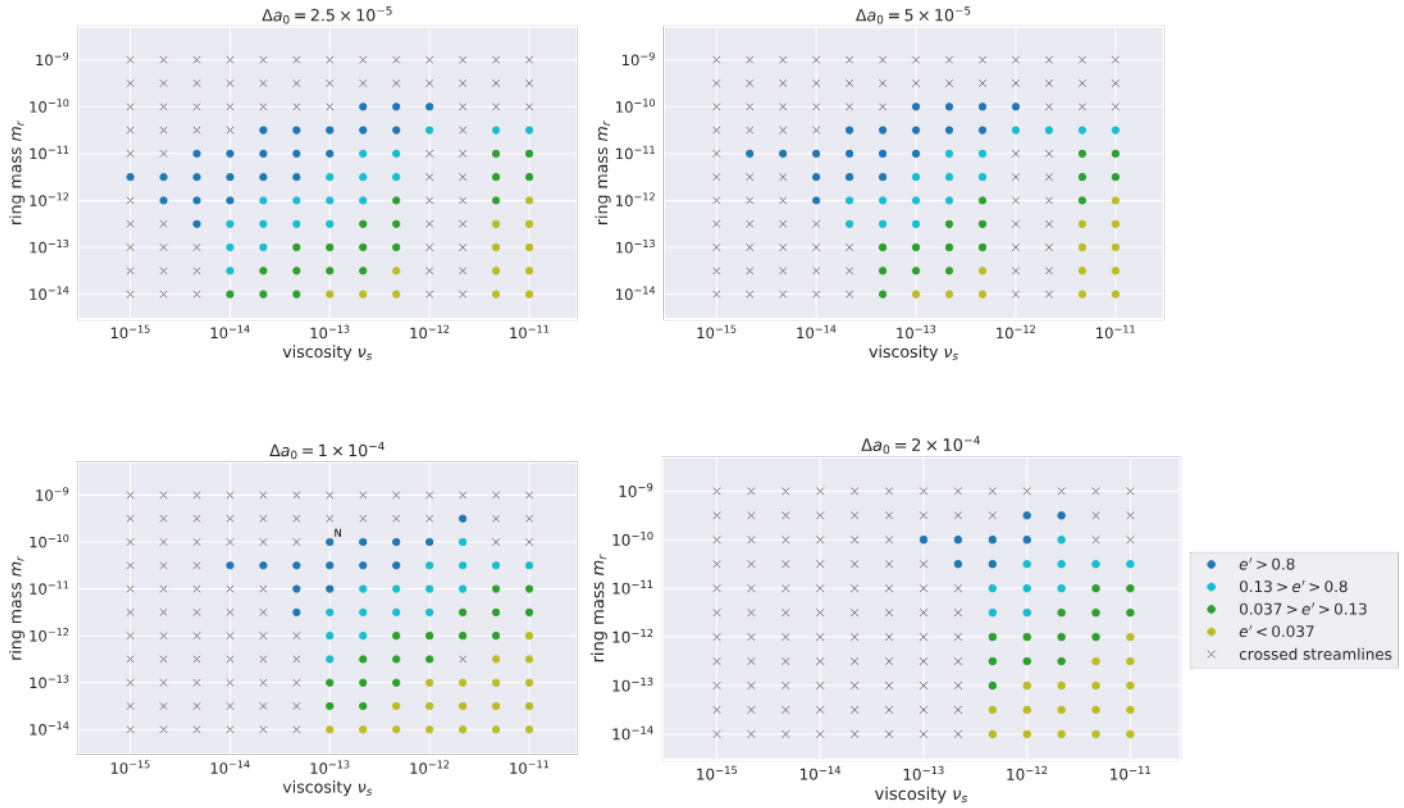

Figure 15. Outcomes for 572 ringlet simulations having a variety of ringlet masses m_r and shear viscosities ν_s, with each panel showing results for those ringlets having the same initial radial width $\Delta a = 2.5 \times 10^{-5}$, 5×10^{-5}, 1×10^{-4}, or 2×10^{-4}. Circles indicate those ringlets that evolve into the self-confining state, while an $\times$ indicates those simulations that terminate early when an epi_int_lite particle crossed an adjacent streamline, and *N* indicates the nominal ringlet simulation. The color of each self-confining ringlet shows whether the ringlet settled into a high-eccentricity gradient state with $e' > 0.8$ blue), or smaller eccentricity gradients $0.13 > e' > 0.8$ cyan), $0.037 > e' > 0.13$ green), or $e < 0.037$ yellow). ll simulations are evolved for the greater of 10 dynamical timescales $\tau_{\rm dyn}$ or 10 viscous timescales τ_ν.

where circles indicate those ringlets that do evolve into a self-confining state. ll simulations of self-confining ringlets are evolved in time until $10\tau_{\rm dyn}$, where the so-called dynamical time $\tau_{\rm dyn}$ is the moment when the ringlet's nonlinearity parameter q first exceeds 0.6, since Figure 7 suggests that $10\tau_{\rm dyn}$ is sufficient time to assess whether the ringlet has truly arrived at the self-confining state.

The $\times$ simulations in Figure 15 terminated early when an epi_int_lite particle crossed a neighboring streamline. In reality, strong pressure forces would have developed as adjacent streamlines converged and enhanced particle densities and particle collisions, with ring particles possibly rebounding off this high-density region and/or splashing vertically, none of which is accounted for with this version of epi_int_lite. So, this survey simply terminates all such simulations and flags that occur with an $\times$ in Figure 15. Keep in mind though that this does not mean that those particular ringlets would not have evolved into a self-confining state. Instead, the streamlines in these ringlets have evolved so close to each other that a more sophisticated and possibly nonlinear treatment of pressure effects would have been needed in order to accurately assess their fates.

Each circle in Figure 15 represents a self-confining ringlet whose nonlinearity parameter settles into a value that is close to the anticipated value, $q \simeq 0.9$. But these self-confining ringlets' final eccentricity gradients e' also settle into a spectrum of values, $0 \leqslant e' \leqslant 0.9$, with outcomes indicated by circle color in Figure 15: blue for a high-eccentricity gradient ringlets having $e' > 0.8$, cyan for smaller eccentricity gradients $0.13 > e' > 0.8$, green for $0.037 > e' > 0.13$, and yellow for very low eccentricity gradients $e\mathfrak{d} < 0.037$, with these intervals chosen so that there are approximately 60 simulations in each color bin. Inspection of Figure 15 also shows that ringlets having lower e' have lower masses and higher viscosities than the higher e' ringlets.

Figure 16 shows how eccentricity gradient varies over time $t/\tau_{\rm dyn}$ for a sample of self-confining ringlet simulations. This figure also shows that the range of simulated e' outcomes also agrees with the range of eccentricity gradients observed among several of Saturn's more well-studied narrow eccentric ringlets, namely the Maxwell, Titan, and Laplace ringlets, whose e' are indicated by the black horizontal lines. Figure 16 also shows there is a pileup of simulated outcomes near Laplace's eccentricity gradient $e' \simeq 0.04$, as well as a dearth of simulations at significantly lower values of e'. Which indicates that the Huygens ringlet, whose $e' \lesssim 0.01$, cannot be accounted for by the self-confining mechanism considered here.

lso keep in mind that Figure 16 is not an apples-to-apples comparison of simulated ringlets to observed ringlets, since no attempt is made here to match the observed ringlet's semimajor axis width Δa to the simulated ringlet's final Δa. Rather, Figure 16's main point is that many of the observed narrow eccentric ringlets that have $e' \gtrsim 0.04$ are consistent with this model of a viscous self-gravitating ringlet that is also self-confining. Finally, recall that $q = \sqrt{e' \quad \tilde{\omega}'}$, which tells us that lower eccentricity gradient ringlets have a larger periapse twist $|\tilde{\omega}'|$.

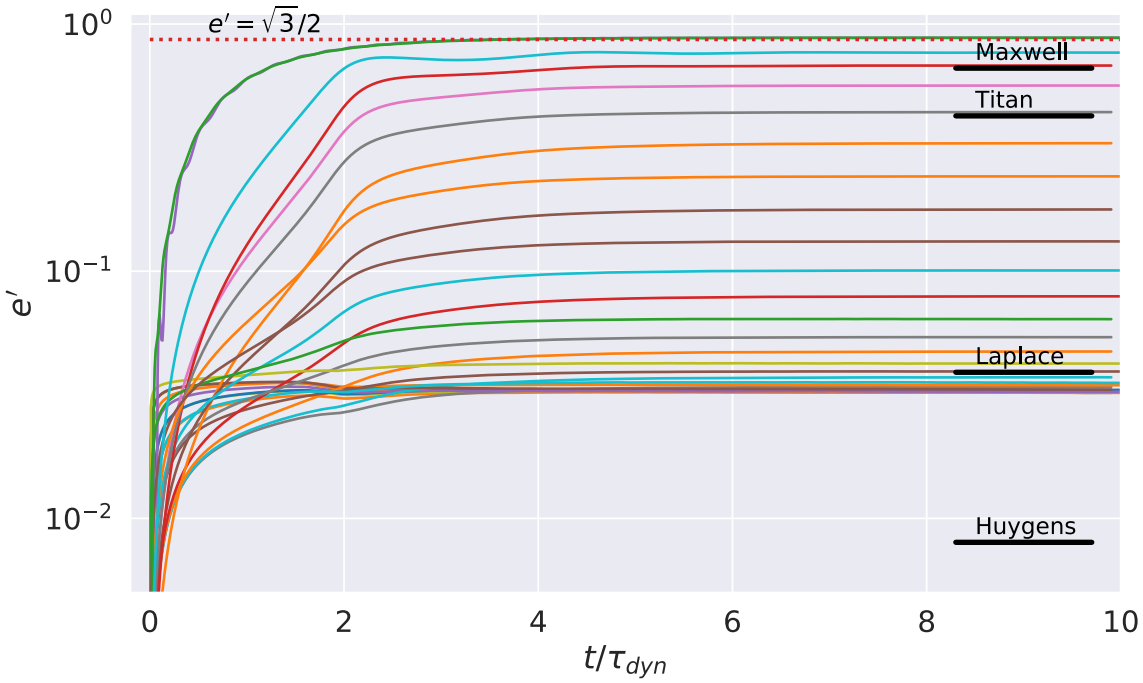

Figure 16. Eccentricity gradient e' vs. time $t/\tau_{\rm dyn}$ for a sample of 28 self-confining ringlets such that their eccentricity gradients e' span the range of values exhibited by the simulations reported in Figure 15. The ringlet's dynamical timescale $\tau_{\rm dyn}$ is the time the when its nonlinearity parameter q exceeds 0.6. Sample ringlets have initial $2.5 \times 10^{-5} \leqslant \Delta a \leqslant 2.0 \times 10^{-4}$, $10^{-14} \leqslant m_r \leqslant 10^{-10}$, and $10^{-14} \leqslant \nu_s \leqslant 10^{-11}$. Horizontal black lines indicated the observed eccentricity gradients exhibited by the Maxwell, Titan, Laplace, and Huygens ringlets at Saturn P. D. Nicholson et al. 2014, R. G. French et al. 2016b, J. N. Spitale & J. M. Hahn 2016). The dotted line is the $e' = \sqrt{3}$ threshold.

We also note R. G. French et al.'s 2024) study of the Uranian ringlets abbreviated here as F24) which reports observed values for e' and $\tilde{\omega}'$ for nine ringlets; see quantities $q_{em} = e'$ and $q_{\tilde{\omega}m} = \tilde{\omega}'$ for the $m = 1$ rows in Table 14 of F24. Nearly all of the ringlets monitored in F24 have nonlinearity parameters $q = \sqrt{q_{em}^2 \quad q_{\tilde{\omega}m}^2} < 0.66$ that are significantly smaller than the $q \simeq 0.9$ achieved by the self-confining ringlets simulated here.[7] From this, we conclude that the Uranian ringlets are unlike those simulated here.

4.5.1. Variations with Ringlet Viscosity

Figure 17 shows the periapse twist $\tilde{\omega}' \simeq ea\Delta\tilde{\omega}$ Δa versus time for six ringlets having the same initial e_0, Δa, m_r and ν_b as the nominal ringlet but with differing shear viscosities ν_s, and that plot shows that twist $|\tilde{\omega}'|$ varies with ν_s. This indicates that if the twist $|\tilde{\omega}'|$ could be observed in a self-confining ringlet, then the ringlet's viscosity could then be inferred.

4.5.2. Variations with Initial Eccentricity

dditional simulations illustrate how outcomes depend upon the ringlet's initial eccentricity e_0. Figure 18 shows seven simulations of the nominal ringlet that all have identical physical properties mass m_r, viscosity ν_s, and initial width Δa) but differing initial e_0 ranging over $0 \leqslant e_0 \leqslant 0.04$. That plot shows that higher-e ringlets settle into the self-confining state sooner than the lower-e ringlets. This is because the higher-e ringlet's secular gravitational perturbation of itself drives its eccentricity gradient, and hence q, toward $q \simeq \sqrt{3}$ faster than the lower-e ringlets. Consequently, higher-e ringlets tend to be narrower than lower-e ringlets because they will have had less time to spread before settling into self-confinement. lso note that the $e_0 = 0$ ringlet blue curve) experiences zero secular gravitational perturbations, so its q is always zero and is destined to spread forever.

The next subsection will examine the rate at which a self-confining ringlet's eccentricity e decays over time due to viscosity, and all ringlets shown in Figures 1–16 have eccentricities e that decay at the expected rates.

4.6. Eccentricity Damping

Viscous friction within the ringlet is a result of dissipative collisions among ringlet particles. Particle collisions generate heat that is radiated into space, and the source of that radiated energy is the ringlet's total energy $E_r = -m_r GM/2a + E_{\rm sg}$, where m_r is the ringlet's total mass, a its semimajor axis, and $E_{\rm sg}$ is the ringlet's energy due to its self-gravity, which is constant when the ringlet is self-confining. Collisions conserve angular momentum, so the ringlet's total angular momentum $L_r = m_r\sqrt{GMa \quad - e^2)}$ is constant, so $dL_r/dt = 0$ implies that

$$\frac{de^2}{dt} \simeq -\frac{}{a}\frac{da}{dt} \qquad 23)$$

to lowest order in the ringlet's small eccentricity e. The ringlet's energy dissipation rate is $\dot{E}_r = dE_r\ dt = m_r GM\dot{a} \quad a$ so $\dot{a} \simeq \dot{E}_r \ m_r a\Omega$ and

$$\frac{de^2}{dt} \simeq \frac{2\dot{E}_r}{m_r a^2\Omega^2} \qquad 24)$$

[7] The exception F24) is Uranus' β ringlet whose $q \simeq 1.2$ is so large as to imply that this ringlet is very disturbed, its streamlines are crossing e.g., N. Borderies et al. 1982), and that ring particles are crashing into each other.

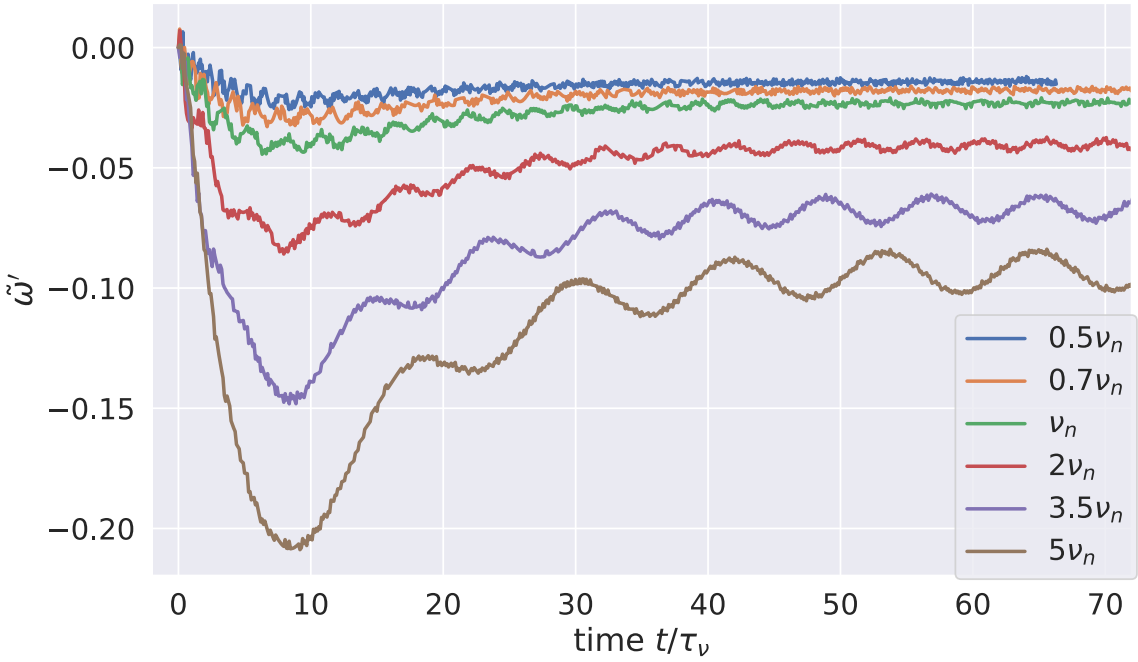

Figure 17. Periapse twist $\tilde{\omega}'$ is plotted vs. time t/τ_ν for six ringlets having the same initial e_0, Δa, m_r as the nominal ringlet but differing shear viscosities ν_s that range over $0.5\nu_n \leqslant \nu_s \leqslant 5\nu_n$, where $\nu_n = 1.0 \times 10^{-13}$ is the nominal ringlet's shear viscosity. The time evolution of these ringlets' other orbit elements, Δa, e, e', and q, are very similar to those exhibited by the nominal ringlet, Figures 2–7.

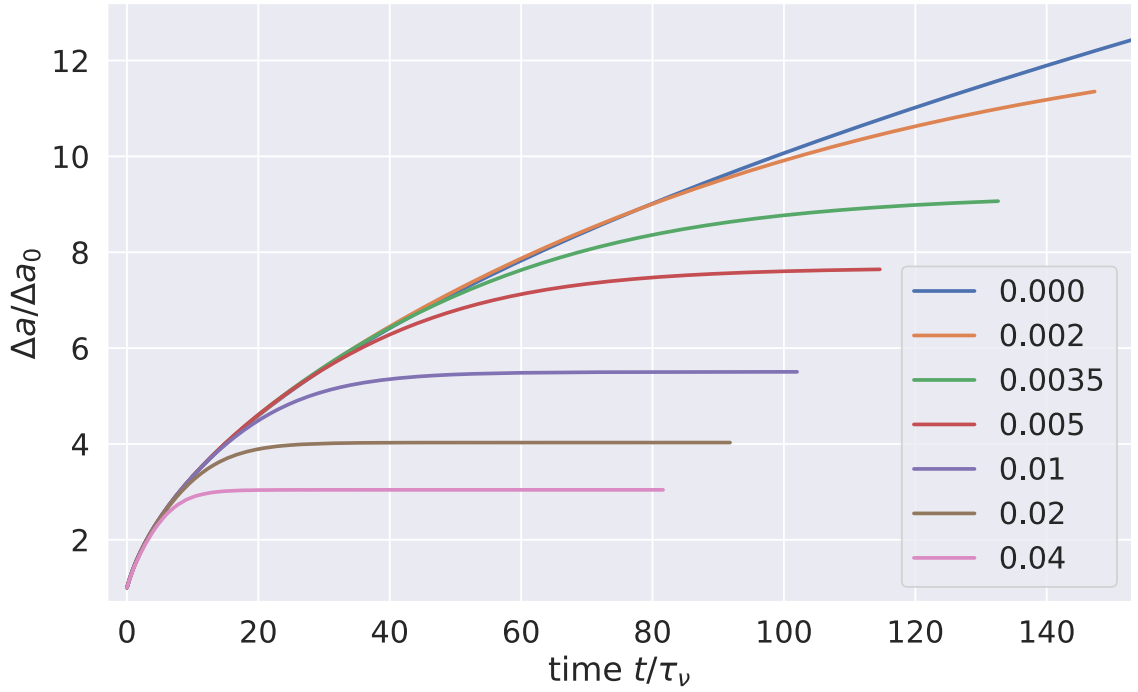

Figure 18. Simulations of seven nominal ringlets having a variety of initial eccentricities $0 \leqslant e_0 \leqslant 0.04$. Curves show each ringlet's semimajor axis width Δa in units of its initial Δa_0 vs. time t/τ_ν, and show that higher-e ringlets settle into self-confinement sooner than the lower-e ringlets.

where $GM \simeq a^3\Omega^2$ to lowest order in J_2. lso note that the surface area of energy dissipation within a viscous disk is

$$\delta = -\nu_s \sigma \; r\omega')^2 \qquad 25)$$

J. E. Pringle 1981), where $\omega = v_\theta/r$ is the angular velocity and $\omega' = \partial\omega \;\; \partial r$ its radial gradient.

Now consider a small tangential segment within the ringlet whose length is $d\ell = rd\varphi$, where φ is the segment's longitude measured from the ringlet's periapse and $d\varphi$ is the small segment's angular extent. The segment's area is $d \;\; = \Delta r d\ell = r\Delta r d\varphi$, where Δr is the ringlet's radial width. The rate at which that patch's viscosity dissipates orbital energy is $d\dot{E}_r = \delta d \;\;$, so the ringlet's total energy dissipation

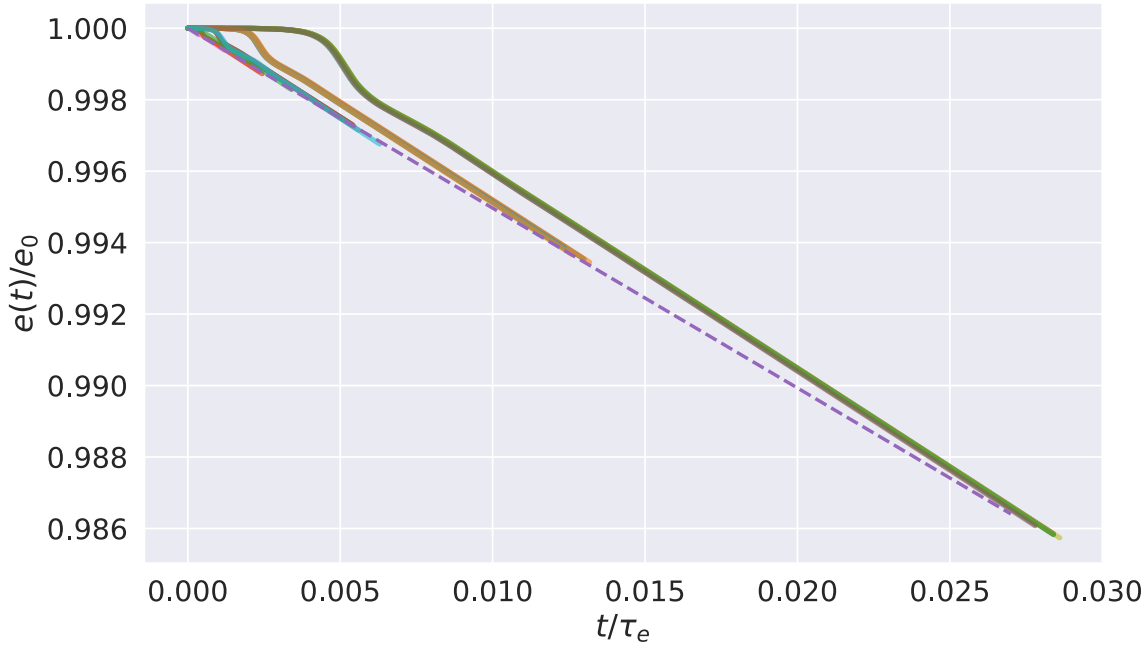

Figure 19. Plot of $e\ t)/e_0$ vs. time t/τ_e for the sample of 28 simulations shown in Figure 16, while the dashed curve is the expected behavior, Equation 29). This sample of simulations have τ_e ranging over $2.5 \times 10^6 \leqslant \tau_e \leqslant 2.5 \times 10^9$.

rate is $\dot{E}_r = \oint d\dot{E}_r$ when integrated about the ringlet's circumference, and so $\dot{E}_r = -2\nu_s \lambda \int^{\pi} r^3 \omega'^2 d\varphi$ since the ringlet's linear density $\lambda = \sigma \Delta r \simeq m_r/2\pi a$. So, the total energy loss rate due to ringlet viscosity becomes

$$\dot{E}_r \simeq -\frac{9}{4} I\ e')m_r \nu_s \Omega \qquad 6)$$

when Equation 11) is used to replace ω', and the integral

$$I\ e') = \frac{1}{\pi}\int_0^{\pi} \left(\frac{1 - \frac{4}{3}e' \cos\varphi}{1 - e' \cos\varphi}\right)^2 d\varphi. \qquad 27)$$

Note that $I\ e')$ is of order unity except when e' is very close to 1, and numerical evaluation shows that $I\ e') \simeq 0.889$ when $e' = \sqrt{3}$.

Inserting Equation 26) into 24) then yields the rate at which e^2 is damped,

$$\frac{de^2}{dt} = -\frac{9I\nu_s}{2a^2} \qquad 28)$$

which is easily integrated to obtain

$$e\ t) = e_0\sqrt{1 - \frac{t}{\tau_e}} \qquad 29)$$

where e_0 is the ringlet's initial eccentricity and

$$\tau_e = \frac{2a^2 e^2}{9I\nu_s} \qquad 3\ )$$

is the ringlet's eccentricity damping timescale. These expectations are also confirmed in Figure 19, which plots $e\ t)/e_0$ versus time t/τ_e for the sample of 28 simulations shown in Figure 16, with the dashed curve indicating the theoretical predictions of Equations 29) and 30). That all simulated curves have slopes similar to the dashed line tells us that Equations 29) and 30) are good indicators of outcomes across a wide variety of ringlet parameters.

So viscosity circularizes the ringlet in time τ_e, during which time the ringlet's semimajor axis will have shrunk by $\Delta a = \dot{a}\tau_e = -e^2 a$ by Equations 23) and 28), so the ringlet's fractional drift inwards due to viscous damping is

$$\frac{\Delta a}{a} = -e_0^2 \qquad 31)$$

which is small. nd after the ringlet's inner edge damps to zero, its eccentricity gradient e' will then shrink over time, angular momentum flux reversal will diminish, and the ringlet's viscous spreading will resume. So self-confinement of narrow eccentric ringlets is only temporary after all, until time τ_e has elapsed, which is $\tau_e/2\pi \sim 1.6 \times 10^6$ orbits for the nominal model considered here, which is only $\sim 10^3$ yr for a ringlet orbiting at $a \sim 10^{10}$ cm about Saturn. Recall from Section 3.1 that the viscous lifetime of a non-self-confining nominal ringlet is only $\tau_\nu/2\pi \sim 500$ orbits, so self-confinement evidently extends the lifetime of a narrow eccentric ringlet by an additional factor of $\sim$3000. But self-confinement does not solve the ringlet's lifetime problem because self-confinement is ultimately defeated by viscous damping of the ringlet's eccentricity.

4.7. Number of Streamlines N_s

When the simulated ringlet is composed of $N_s = 2$ streamlines, the ringlet's evolution is largely analytic see N. Borderies et al. 1982, 1983a), and the analytic predictions provide excellent benchmark tests for the epi_int_lite integrator. This subsection assesses whether the results obtained for the simpler $N_s = 2$ ringlet also apply to more realistic ringlets having $N_s > 2$.

Figures 20 and 21 recompute the nominal ringlet's evolution for ringlets having a range of streamlines, $2 \leqslant N_s \leqslant 14$, all of

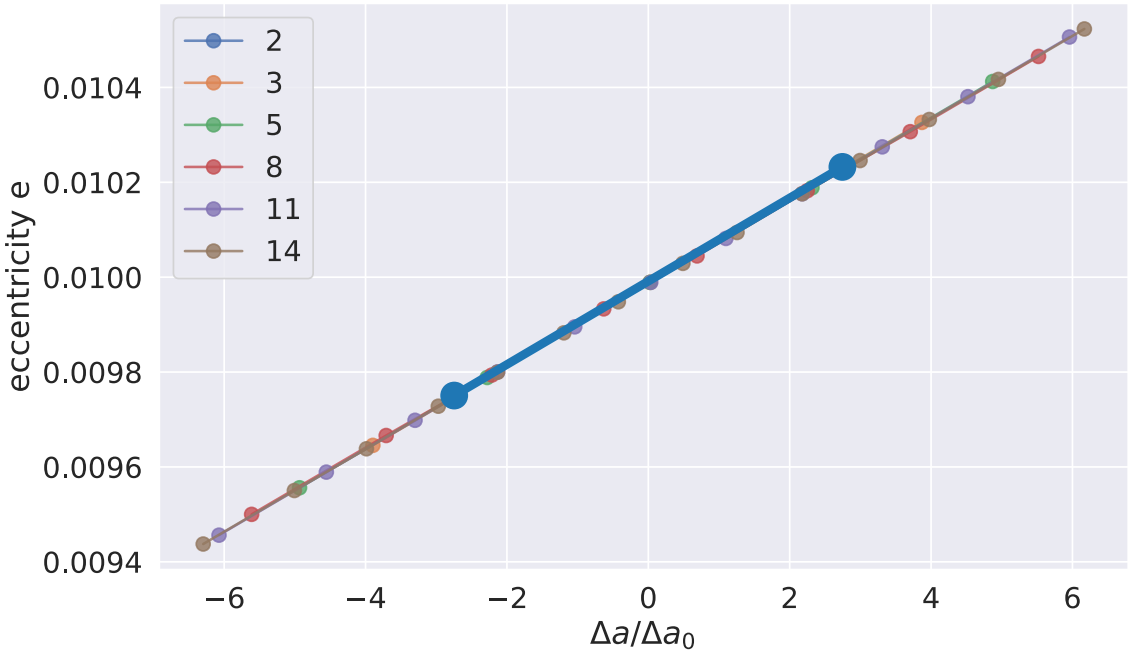

Figure 20. suite of ringlets is evolved, these ringlets have the same properties as the nominal ringlet except they contain varied numbers of streamlines $2 \leqslant N_s \leqslant 14$, with N_s indicated by the plot legend. Simulated ringlets' final eccentricities e are plotted vs. their relative semimajor axis $\Delta a = a - \bar{a}$, where $\bar{a}$ is the ringlet's mean semimajor axis.

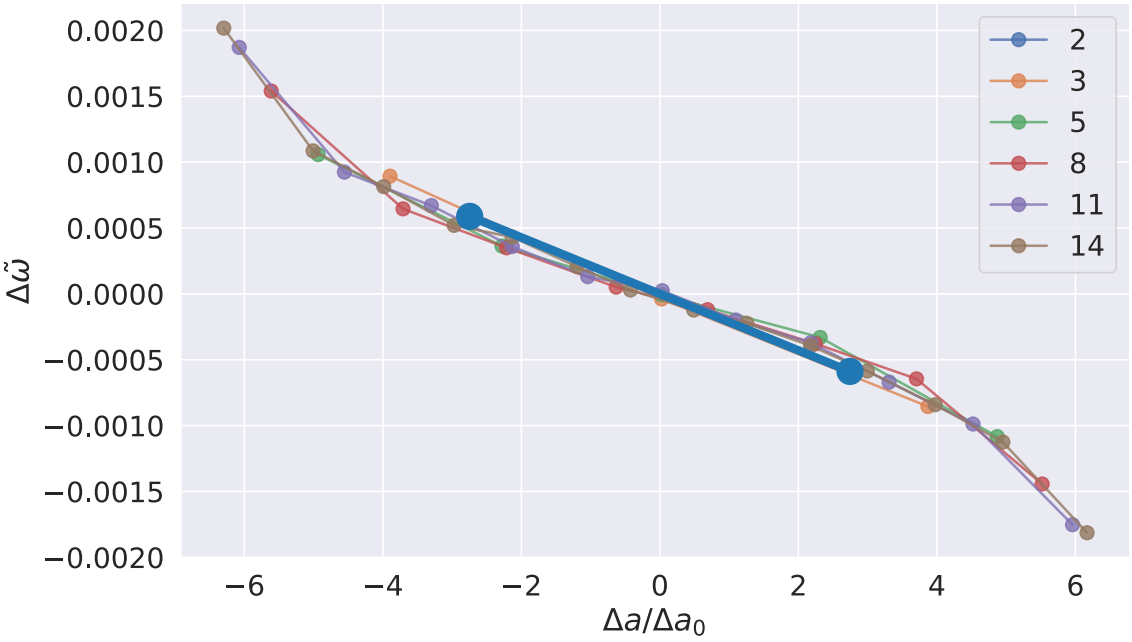

Figure 21. Simulated ringlets' final relative longitudes of periapse $\Delta\tilde{\omega} = \tilde{\omega} - \bar{\omega}$ are plotted vs. their relative semimajor axis $\Delta a = a - \bar{a}$, where $\bar{a}$ is the ringlet's mean semimajor axes and $\bar{\omega}$ is their mean longitude of periapse, and the number of streamlines N_s is indicated in the plot legend.

which have q-evolution very similar to that exhibited by the $N_s = 2$ simulation seen in Figure 7. Figure 20 plots each streamline's eccentricity e versus their relative semimajor axis $\Delta a = a - \bar{a}$, which shows that all simulated ringlet's have the same eccentricity gradient e' regardless of the number of streamlines N_s. Ditto for the ringlets' relative longitudes of periapse, $\Delta\tilde{\omega}$ when plotted versus Δa, Figure 21, which shows that all simulated ringlets have comparable gradients in $\tilde{\omega}$. The only noteworthy difference seen here is that the smaller $N_s \leqslant 3$ simulations do not resolve the extra periapse twist that is seen at the edges of the higher-resolution simulations. Except for this one distinction, the evolution of the $N_s > 2$ ringlets is very similar to that exhibited by nominal ringlet composed of $N_s = 2$ streamlines.

4.7.1. Surface Densities and Sharp Edges

The main shortcoming of the $N_s = 2$ simulation is that it reveals nothing about a ringlet's possible sharp edges, since a two-streamline ringlet always has artificially sharp edges. To examine this further, Figure 22 shows the radial surface density profile along the periapse direction for the $2 \leqslant N_s \leqslant 14$

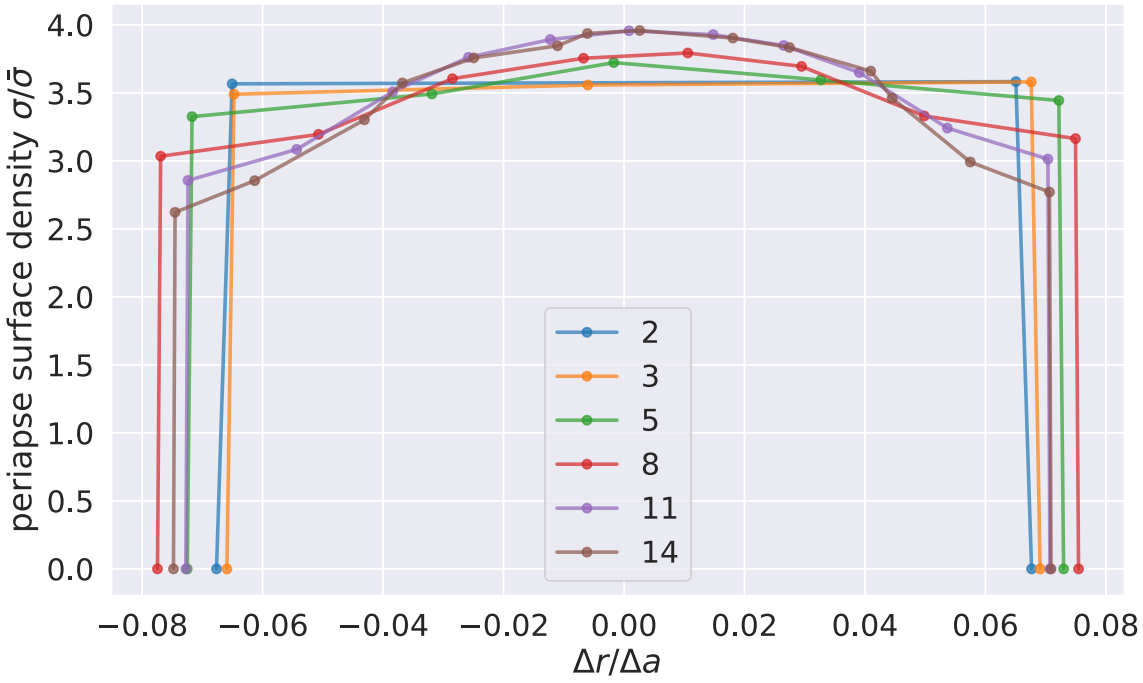

Figure 22. Radial surface density profiles σ Δr) of the $2 \leqslant N_s \leqslant 14$ ringlets of Section 4.7 plotted along the ringlets' direction of periapse. Surface density σ is shown in units of the ringlet's mean surface density $\bar{\sigma}$, and radial distance $\Delta r = r - r_{\rm mid}$ is measured relative to chord's midpoint and in unit of the ringlet's semimajor axis width $\Delta a = a_{\rm outer} - a_{\rm inner}$.

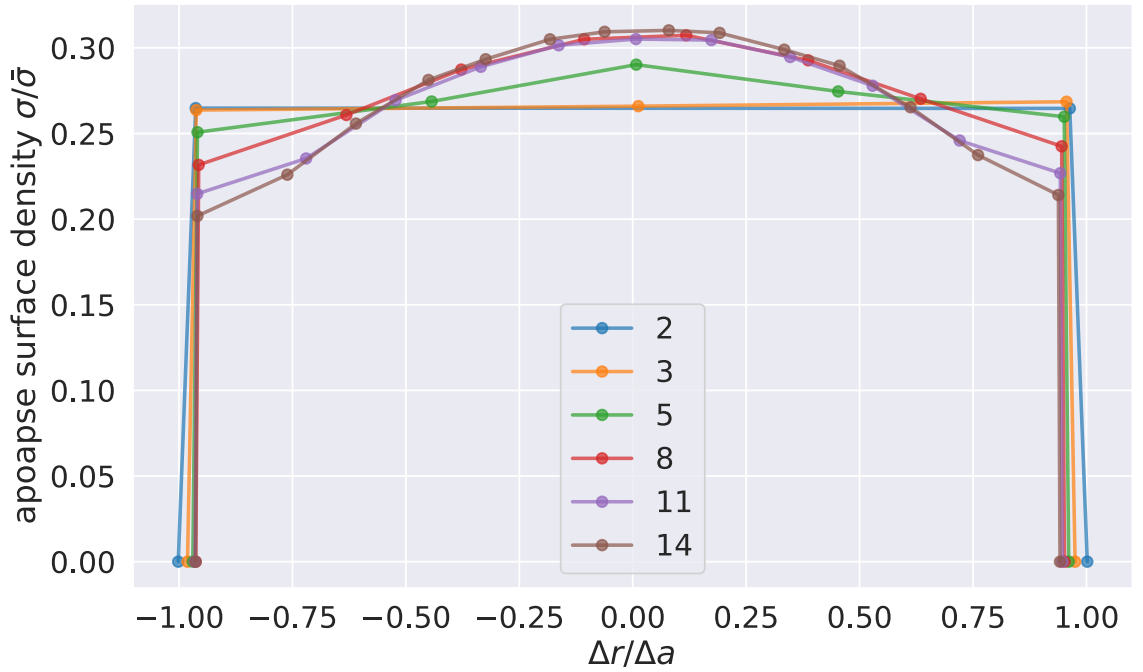

Figure 23. Radial surface density profiles σ Δr) of the $2 \leqslant N_s \leqslant 14$ simulations, plotted along the ringlets' direction of apoapse. Note that the ringlets' apoapse surface densities are about 13 times smaller than their periapse σ, Figure 22, because they are also wider by that amount.

ringlets that were simulated in Section 4.7. This plot shows that all of the ringlets' edges are sharp after they arrive in the self-confining state, regardless of N_s. When self-confining, each streamline is approximately equidistant within 25%) from their neighbors, which causes ringlet surface density σ to remain constant within 25%) in the ringlet's interior, which then plummets to zero beyond the ringlet's boundaries. Ditto for the surface density profiles seen along the ringlets' apoapse direction; see Figure 23. In summary, the self-confining ringlet examined here has a smooth radial surface density profile that is concave-down, with surface density maxima at the ringlet's center, and has sharp edges.

Note that if a viscous ringlet were instead unconfined, then its positive angular momentum flux would have repelled the edgemost streamlines away from the interior streamlines, which in turn would have caused the ringlet's concave-down surface density profile to taper smoothly to zero at its edges, as is seen in Figure 1 of J. E. Pringle 1981). Meanwhile, the

other ringlet models, those that rely on unseen shepherd satellites to maintain confinement, all exhibit smooth surface densities having a variety of concavities, yet all have sharp edges P. Goldreich & S. Tremaine 1979a; E. I. Chiang & P. Goldreich 2000; I. Mosqueira & P. R. Estrada 2002).

In comparison, the Maxwell ringlet's radial optical depth profiles can be approximately described as concave-downish with a spiral density wave riding on top P. D. Nicholson et al. 2014). The Titan ringlet is opaque, so its concavity is unknown, but it does have sharp edges P. D. Nicholson et al. 2014). The Huygens ringlet, which has a tiny eccentricity gradient, is concave-up with sharp edges R. G. French et al. 2016b), while the Laplace ringlet is possibly concave-down with sharp edges and lots of internal structure. The main point is that all well-observed narrow eccentric planetary ringlets have a radial optical depth structure that is much more complicated than is exhibited by published models to date.

5. Self-confining Ringlet Origin Scenario

Here, we use the preceding results to speculate about the origin of narrow eccentric planetary ringlets. If such ringlets are truly self-confining, then they are extremely young, only $\sim\mathcal{O}$ 1) yr old per Equation 30) and Section 4.6. Our preferred least-speculative origin scenario which is still quite speculative) proposes that the ringlet precursor was originally an especially large ring particle that was orbiting elsewhere, such as within a nearby dense planetary ring, presumably as an embedded moonlet aka propeller M. S. Tiscareno et al. 2010). If that embedded moonlet happened to form near the edge of the dense planetary ring, then the moonlet's reaction to the shepherding torque that it exerts across the dense ring which is $-1\times$ the radial integral of Equation 71) of P. Goldreich & S. Tremaine 1982) would cause that moonlet to migrate toward and then beyond the ring's edge. nd if a dense planetary ring can spawn one such moonlet, it can also spawn additional moonlets. S. Charnoz et al. 2010) also propose this for the origin for all the small satellites orbiting just beyond Saturn's ring, i.e., tlas, Prometheus, Pandora, Epimethius, and Janus.

moonlet's radial migration rate due to the ring-shepherding torque also varies with moonlet mass, so a larger moonlet will eventually overtake a smaller moonlet that is orbiting beyond it. Indeed, calculations by F. Poulet & B. Sicardy 2001) suggest that satellite Prometheus emerged from the outer edge of Saturn's ring $\sim 10^7$ yr ago, and that it will have a close encounter with the smaller satellite Pandora that is currently orbiting just exterior to Prometheus in another $\sim 10^7$ yr. Multiple close moonlet–moonlet encounters would then pump up moonlet eccentricities until they collide. If that collision is sufficiently vigorous to disrupt one or both moonlets, then a narrow eccentric planetary ringlet composed of collisional debris would result. Viscous particle–particle collisions would then cause that young ringlet to spread radially Figure 2) while its self-gravity would pump up its eccentricity gradient Figure 7), which, if sufficiently vigorous, would cause it to settle into the self-confining state that is sharp-edged Figure 23) like most observed narrow eccentric ringlets. Nonetheless, self-confinement is temporary and lasts only $\sim\mathcal{O}$ 1) yr due to the ringlet's viscosity damping its eccentricity until its inner edge gets circularized. Which would cause the ringlet's q to drop below the $q \simeq \sqrt{3}$ 2 threshold for self-confinement, the ringlet would again spread radially, and its edges would lose their sharpness.

So, in summary, this purportedly least-speculative ringlet origin scenario implies that dense planetary rings are frequently forming and emitting small embedded moonlets that then migrate away, due to their gravitational shepherding of that ring, toward and then beyond the nearby ring-edge where they are later disrupted after colliding with other such moonlets. The resulting debris quickly shears out into a low-eccentricity ringlet whose self-gravity excites its eccentricity gradient until it settles temporarily into the self-confining state, which is sharp-edged. The next step in any assessment of the viability of this least-speculative ringlet origin scenario would require an estimate of the various timescales that are relevant here, namely, the moonlet's formation timescale, the moonlet's migration timescale, its lifetime versus collisional disruption, and the ringlet's self-confinement lifetime, to confirm that none of these lifetimes are so long as to cast doubt on this ringlet origin scenario. This more detailed analysis is deferred to a follow-up study.

6. Summary of Findings

Our main findings are as follows:

1. Simulations show that viscous self-gravitating narrow eccentric ringlets having a wide variety of initial physical properties mass, width, and viscosity) do evolve into the self-confining state Figure 15).
2. Self-gravity causes a self-confining ringlet's nonlinearity parameter q, which is the rms sum of the ringlet's dimensionless eccentricity gradient $e' = ade\ da$ and its dimensionless periapse twist $\tilde{\omega}' = ead\tilde{\omega}\ da$, to grow over time until it exceeds the $q \simeq \sqrt{3}$ 2 $\simeq 0.866$ threshold where the ringlet's orbit-averaged angular momentum flux due to ringlet viscosity + self-gravity reversal is zero.
3. Gravitating ringlets that are self-confining have small but positive i.e., radially outwards) viscous angular momentum luminosity that is counterbalanced by their negative gravitational angular momentum luminosity Section 4.3). Ringlet self-gravity is also the reason for a self-confining ringlet having nonlinearity parameter $q \simeq 0.9$ that is slightly larger than the $q = \sqrt{3} \simeq 0.866$ threshold that is expected of a viscous nongravitating ringlet N. Borderies et al. 1982).
4. Simulated ringlets that do settle into self-confinement have final eccentricity gradients $0.04 \lesssim e' \lesssim 0.9$; see Figure 16. Since all such ringlets have $q \simeq 0.9$, this means that ringlets having smaller eccentricity gradients e' also have larger periapse twist $|\tilde{\omega}'|$ that is likely due to a higher ringlet viscosity Section 4.5.1).
5. The ringlet's total energy luminosity $\mathcal{L}_E$ is zero after the ringlet has settled into the self-confining state Section 4.4). The ringlet's gravitational energy luminosity $\mathcal{L}_{E\ g}$ is also zero at all times, consistent with secular theory.
6. Self-confining ringlets have sharp edges Section 4.7.1).
7. Ringlet viscosity also circularizes the ringlet in time $\tau_e \sim 10^6$ orbits $\sim$1000 yr Section 4.6). fter viscosity has reduced the eccentricity of the ringlet's inner edge to zero, the ringlet's eccentricity gradient e' will then shrink over time, its angular momentum flux reversal will cease,

and viscous spreading will resume as ringlet viscosity again transmits an outwards flux of angular momentum. Ringlet circularization thus causes it to again resume spreading radially and the ringlet would lose its sharp edges.

8. Self-confining narrow eccentric planetary ringlets are short lived unless there is a mechanism that can pump up the ringlet's eccentricity.
9. We speculate that a sharp-edged self-confining narrow eccentric planetary ringlet first originated as an exceptionally large ring particle orbiting within a nearby dense planetary ring. Possibly as a small embedded moonlet such as the presumed cause of the propeller structures seen in Saturn's main ring. If that embedded moonlet is orbiting near the dense ring's edge, then its reaction to the gravitational shepherding torque that it exerts across the dense ring would cause that moonlet to migrate toward and then beyond the dense ring's edge. If so, then a dense planetary ring can also birth multiple such moonlets. The ring-torque would also cause the largest moonlet to overtake any smaller migrating moonlets, which will encourage moonlet–moonlet scattering and eventual collision. disruptive moonlet collision would generate debris that would quickly shear out into a low-eccentricity ringlet whose self-gravity could excite its eccentricity gradient until it settles into the self-confining state that is sharp-edged, albeit temporarily.

7. dditional Follow-up Studies

Here, we list possible follow-up studies that could also be pursued using the epi_int_lite streamline integrator:

1. *Nonlinear spiral density waves*. nalytics theories exist, but they are complex and challenging to employ F. H. Shu et al. 1985; N. Borderies et al. 1986), whereas some might regard the execution of an epi_int_lite simulation as the simpler/faster way forward. Spiral density waves are nonlinear when the surface density variation due to the wave is comparable to the ring's undisturbed surface density i.e., $|\Delta\sigma| \sim \sigma_0$. Since $\sigma = \lambda/\Delta r$, this means that streamline separation Δr need only shrink by a factor of two to make a density wave nonlinear. Note that eccentricities associated with the wave are still small, which means that the streamline-integrator approach is well suited for simulating nonlinear density waves. See for example the R. G. French et al. 2016a) simulation of a marginally nonlinear spiral density wave using the epi_int code, which is the predecessor of epi_int_lite.
2. *Partly incompressible nonlinear spiral density waves*. One can imagine that a sufficiently vigorous nonlinear density wave could drive particle densities high enough such that ring particles in the affected region are packed shoulder-to-shoulder so that further compaction is impossible because that region has become incompressible. We suspect that these incompressible patches could also result in shocks and/or vertical splashing as the wave drives additional ring particles into the affected regions. Which surely would alter the wave's dynamics and may lead to new and possibly observable phenomena e.g., N. Borderies et al. 1985). Note that the equation of state EOS) employed by epi_int_lite assumes that the ring is a compressible particle gas, but that EOS could easily be adapted to account for the additional forces that would result as particles enter into or recoil from the incompressible patches generated by the wave.
3. *Nonlinear spiral bending waves*. lthough theories for nonlinear spiral density waves do exist, an analytic theory for a nonlinear spiral bending wave does not. The fundamental assumption of linearized bending wave theory is that the radial forces associated with the wave are negligible compared to the wave's vertical forcing of the ring F. H. Shu 1984). Which is true provided the bending wavelength λ_b is large compared to the bending wave amplitude , which is the ring plane's maximal vertical displacement due to the bending wave, i.e., $\lambda_b \gg$. lthough the epi_int_lite streamline integrator is currently a two-dimensional code, adapting it to the third dimension should be straightforward, which means that the revised code would then be well positioned to simulate a nonlinear spiral bending wave having $\lambda_b \lesssim$. lso note that, when in this regime, the gravitational forces exerted by the warped ring plane are no longer purely vertical, i.e., the wave's forcing of the warped ring plane within distances $\sim\lambda_b$ will also have an in-plane component, and that radial forcing of a self-gravitating ring tends to beget spiral density waves. Which suggests that a spiral bending wave, whose wavelength λ_b shrinks as it propagates, will eventually go nonlinear in a way that might spawn a spiral density wave that could be observable in Cassini observations of Saturn's rings.
4. *Galactic spiral structure*. The main difference between planetary and galactic trajectories is in their precession rates. Planetary orbits precess slowly, $|\dot{\tilde{\omega}}| = |\Omega - \kappa| \ll \Omega$, whereas galactic trajectories, which can also be described by equations like Equation 9), precess rapidly, $|\dot{\tilde{\omega}}| \sim \mathcal{O}\ \Omega$). Which suggests that epi_int_lite could also be used to simulate galactic spiral structure when the code is provided with appropriate functions for $\Omega\ r$) and $\kappa\ r$). Epi_int_lite is also quite general in that it can simulate waves in both gravity and pressure dominated disks, and additional perturbations from a central bar would be straightforward to include.
5. *symmetric circumstellar debris disk*. debris disk is a dusty circumstellar disk that is often found in orbit about younger stars, $\sim 10^{7-9}$ yr B. Matthews et al. 2018), and is a possible signature of ongoing planet formation. Many such star-disk systems are suspected of hosting an unseen planetesimal "birth ring," wherein collisions among those planetesimals generates dust whose smaller grains are launched into very wide eccentric orbits due to stellar radiation pressure L. E. Strubbe & E. I. Chiang 2006). Those eccentric dust grains populate a very broad disk that can be observed out to stellar-centric distances of $r \sim 1000$ au when imaged via scattered starlight, which also tends to favor the discovery of edge-on debris disks. These edge-on dust disks' ansae routinely exhibit surface-brightness asymmetries, as well other structures that may be due to gravitational forcing by unseen protoplanets and/or giant impacts into those protoplanets J. W. Jones et al. 2023). Surface-brightness asymmetries can also be due to the birth ring having an eccentricity

J. M. Hahn 2009), which again implicates gravitational forcing by unseen planets or protoplanets, but differential precession due to the protoplanets' gravities will eventually defeat the birth ring's eccentricity unless that is resisted by the ring's self-gravity. The longevity of these possibly eccentric birth rings and their debris disks, which is inferred from their host stars' 10^{7+} yr ages, suggests that these possibly eccentric birth rings can also be very long-lived. Which causes us to wonder whether self-gravity may play a role in preserving a birth ring's structure via the self-confinement mechanism considered here, which epi_int_lite would be well suited to investigate.

The epi_int_lite streamline integrator source code is available on GitHub see footnote 6), and readers are encouraged to reach out if they wish to use that code in their research.

cknowledgments

This research was supported by the National Science Foundation via grant No. ST-1313013. portion of this paper as well as the epi_int_lite integrator were composed and developed while at the Water Tank karaoke bar in northwest ustin TX, and the authors thank proprietor James Stryker for his hospitality. The authors also thank Joe Spitale and the anonymous reviewer for their comments about this work.

ppendix

The drift step implemented in the original epi_int code utilized the epicyclic equations of N. Borderies-Rappaport & P.-Y. Longaretti 1994) to advance an unperturbed particle along its trajectory about an oblate planet. These equations convert a particle's spatial coordinates r, θ, v_r, v_θ into epicyclic orbit elements a e M $\tilde{\omega}$ that are easily advanced by time step Δt, after which the epicyclic elements are converted back to spatial coordinates with an accuracy to $\mathcal{O}$ e). Note though that those epicyclic equations are not reversible, every conversion from spatial to epicyclic coordinates or vice versa also introduces an error of order $\mathcal{O}$ e^3), and the accumulation of those errors causes the orbits of the epi_int particles to slowly drift over time. But that slow numerical drift was not problematic for the relatively short epi_int simulations reported in J. M. Hahn & J. N. Spitale 2013) that evolved Saturn's B ring for typically $\sim 10^4$ orbit periods. However, the viscous self-gravitating ringlets considered here must be evolved for 10^5–10^6 orbit periods in order for self-confinement to occur, and simulations having those longer execution times were being defeated by this orbital drift. The remedy is to derive an alternate set of epicyclic equations that *are* reversible such that the epi_int_lite's drift step will not be a significant source of numerical error.

Begin with the equation of motion for an unperturbed particle in orbit about the central planet,

$$\ddot{\boldsymbol{r}} = -\nabla\Phi \qquad \text{A1)}$$

where the planet's gravitational potential is

$$\Phi = -\frac{GM}{r} - \frac{J_2 GMR^2}{2r^3} \qquad \text{A2)}$$

where M is the planet's mass, R its radius, J_2 its second zonal harmonic due to oblateness, and with higher-order $J_{n>2}$ terms ignored here. The angular part of Equation 1) is

$$\frac{1}{r}\frac{d}{dt}\ r^2\dot{\theta}) = -\frac{\partial\Phi}{\partial\theta} = 0 \qquad \text{A3)}$$

so the particle's specific angular momentum $h = r\ \dot{\theta} = rv_\theta$ is conserved i.e.,

$$\dot{\theta} = \frac{h}{r^2} \qquad \text{A4)}$$

and inserting that into the radial part of Equation 1) yields

$$\ddot{r} = \frac{h^2}{r^3} - \frac{GM}{r^2} - \frac{3J_2 GMR^2}{2r^4}. \qquad \text{A5)}$$

Solving the above to first-order accuracy $\mathcal{O}$ e) ordinarily yields

$$\begin{aligned} r &\simeq a\ 1\ -\ e\cos M) \\ \theta &\simeq \frac{\Omega}{\kappa}\ M \quad 2e\sin M) \quad \tilde{\omega} \\ v_r = \dot{r} &\simeq ea\kappa\sin M \\ v_\theta = r\dot{\theta} &\simeq a\Omega\ 1 \quad e\cos M) \end{aligned} \qquad \text{A6)}$$

where

$$\Omega\ a) = \sqrt{\frac{GM}{a^3}}\left[1 \quad \frac{3}{2}J_2\left(\frac{R}{a}\right)^2\right]^{1\ 2} \qquad \text{A7)}$$

is the particle's mean orbital frequency and

$$\kappa\ a) = \sqrt{\frac{GM}{a^3}}\left[1\ -\ \frac{3}{2}J_2\left(\frac{R}{a}\right)^2\right]^{1\ 2} \qquad \text{A8)}$$

is its epicyclic frequency. In the above, a, e, $\tilde{\omega}$, and $M = \kappa t$ are the epicyclic orbit elements that have errors of order $\mathcal{O}$ e^2). Equations 6) are easily inverted, which would then provide epicyclic orbit elements a, e, $\tilde{\omega}$, and M as functions of the particle's spatial coordinates r, θ, v_r, and v_θ, but applying them here would be even more problematic since the conversion from spatial coordinates to orbit elements would accrue $\mathcal{O}$ e^2) errors during every drift step, which is even worse that the rate at which epi_int's drift step accrues errors.

The remedy is to choose an alternate set of Equations 6) that also solve the equation of motion 1) to the same accuracy while satisfying Equation 4) exactly. Begin with the above expression for the angular coordinate, $\theta = \Omega\ \kappa)\ M \quad 2e\sin M) \quad \tilde{\omega}$, so that $\dot{\theta} = \Omega\ 1 \quad 2e\cos M)$. Then, require the constant $h = r^2\dot{\theta} = a^2\Omega$ be satisfied exactly, which provides the revised expression for r as a function of orbit elements, $r = a\ \sqrt{1 \quad 2e\cos M}$, noting that this expression differs from that in Equation 6) by an amount of order $\mathcal{O}$ e^2) which is this solution's allowed error. It is then

straightforward to complete the revisions to Equation 6):

$$r = \frac{a}{\sqrt{1 \quad 2e\cos M}}$$
$$\theta = \frac{\Omega}{\kappa} M \quad 2e\sin M) \quad \tilde{\omega}$$
$$v_r = \dot{r} = \frac{ea\kappa \sin M}{1 \quad 2e\cos M)^{3\ 2}} = ea\kappa \sin M\left(\frac{r}{a}\right)^3$$
$$v_\theta = r\dot{\theta} = a\Omega\sqrt{1 \quad 2e\cos M} = \frac{a^2\Omega}{r} \qquad \text{A9)}$$

where Ω and κ are Equations 7) and 8) and $M = \kappa t$.

Equation 9) must also be inverted so that the particle's epicyclic orbit elements $a\ e\ \tilde{\omega}\ M$ can be obtained from the particle's spatial coordinates r, θ, v_r, v_θ, which is done via the following:

1. Calculate the particle's specific angular momentum $h = rv_\theta$ and then solve $h^2 = a^4\Omega^2 = GMa[1 + 3J_2/2)\ R/a)^2]$ for the particle's semimajor axis a, which is

$$a = R\ C \quad \sqrt{C^2 - 3J_2\ 2}) \qquad \text{A10)}$$

   where constant $C = h^2/2GMR$.
2. Calculate Ω and κ using Equations 7) and 8).
3. Note that $e\sin M = v_r\ a\kappa)\ a\ r)^3$ and $e\cos M = \frac{}{2}[\ a\ r)^2 - \ ]$, which provides the particle's eccentricity via $e = \sqrt{e\sin M)^2 \quad e\cos M)^2}$ and its mean anomaly M inferred from $\tan M = e\sin M\ e\cos M$.
4. The particle's longitude of periapse is $\tilde{\omega} = \theta - \Omega\ \kappa)\ M \quad 2e\sin M)$.

These equations satisfy the equation of motion 1) to accuracy $\mathcal{O}\ e)$ and with errors of order $\mathcal{O}\ e\ )$. To advance a particle during epi_int_lite's drift step from time t to time $t + \Delta t$, use the above steps 1–4 to convert the particle's spatial coordinates r, θ, v_r, v_θ to epicyclic orbit elements $a\ e\ M\ \tilde{\omega}$, update the particle's mean anomaly via $M \rightarrow \kappa\ t + \Delta t)$, and then use Equation 9) to compute the particle's revised spatial coordinates. nd because steps 1–4 convert coordinates to elements exactly, epi_int_lite's drift step is not a significant source of numerical error.

Finally, we derive the streamlines' angular shear $\partial\omega/\partial r$. The angular velocity $\omega = v_\theta/r = \Omega\ a/r)^2$ by Equation 9) so $\omega \simeq \Omega\ 1 \quad 2e\cos\varphi)$ to first order in e where true anomaly $\varphi = \theta - \tilde{\omega} \simeq M$. Thus, $\partial\omega\ \partial a \simeq -\ 3\Omega\ 2a)\ 1 - \frac{4}{3}e'\cos\varphi)$ since J_2 and e are small though the eccentricity gradient $e' = a\ \partial e\ \partial a)$ might not be small. Likewise, $r \simeq a\ 1 - e\cos\varphi)$ so $\partial r\ \partial a \simeq 1 - e'\cos\varphi$ and so

$$\omega' = \frac{\partial\omega}{\partial r} = \frac{\partial\omega}{\partial a}\ \frac{\partial r}{\partial a} \simeq -\left(\frac{3\Omega}{2a}\right)\frac{1 - \frac{4}{3}e'\cos\varphi}{1 - e'\cos\varphi} \qquad \text{A11)}$$

which interestingly changes sign near periapse, $\varphi \simeq 0$, when the eccentricity gradient is large enough, $e' \gtrsim 3\ 4$.

ppendix B

Write the gravitational angular momentum flux $_{L\,g} = \lambda r\ ^1_{g\,\theta}$ in terms of orbit elements, for a ringlet composed of two streamlines. The one-sided gravitational acceleration that the inner streamline exerts on a particle in the outer streamline is $^1_g = -2G\lambda\ \Delta$. The perturbing streamline's orientation relative to the particle is illustrated Figure 3 of J. M. Hahn & J. N. Spitale 2013), which shows that the particle's tangential acceleration is $^1_{g\,\theta} \simeq -\ v_r\ v_\theta)\ ^1_g$, where v_r and v_θ are the perturbing streamline's radial and azimuthal velocities at the point of minimum separation, where $v_r\ v_\theta \simeq e_0\sin\varphi$ by Equations 9) to first order in the inner streamline's eccentricity e_0 and assuming $\kappa \simeq \Omega$. The inner streamline's orbit elements are designated a_0, e_0, and $\tilde{\omega}$ while the outer streamline has $a_1 = a_0 + \Delta a$, $e_1 = e_0 + \Delta e$, $\tilde{\omega}_1 = \tilde{\omega} \quad \Delta\tilde{\omega}$, and the particle's longitude relative to the inner streamline's periapse is $\varphi \simeq \theta - \tilde{\omega}$. The streamline-particle separation is then

$$\Delta = r_1 - r_0 \simeq\ 1 - e'\cos\varphi - \tilde{\omega}'\sin\varphi)\Delta a \qquad \text{B1)}$$

to first order in the small quantities Δa, Δe, and $\Delta\tilde{\omega}$ and assuming $e \ll e'$, so the gravitation flux of angular momentum at the particle is

$$_{L\,g} \simeq 2eG\lambda^2\left(\frac{a}{\Delta a}\right)\frac{\sin\varphi}{1 - e'\cos\varphi - \tilde{\omega}'\sin\varphi} \qquad \text{B2)}$$

where the streamline's linear density $\lambda = m_1/2\pi a = m_r/4\pi a$ for a streamline whose mass $m_1 = m_r/2$ is half the total ringlet mass m_r.

ppendix C

This appendix compares the evolution of epi_int_lite simulations to theoretical predictions for narrow viscous ringlets, and for narrow gravitating ringlets.

C.0.1. Viscous Evolution

The test described in Figure 24 examines the radial spreading of a narrow viscous nongravitating ringlet. The simulated ringlet has the same physical properties as the nominal ringlet except that it is circular and it has many more streamlines than the $N_s = 2$ simulation of Section 3.1. Each colored curve indicates the ringlet's radial surface density profile $\sigma\ r)$ at various times t. Note that the simulated surface density profiles dashed curves with dots) track nicely with the theoretical prediction solid curves) of J. E. Pringle 1981), which is a good indicator that epi_int_lite is computing the ringlet's viscous evolution correctly.

C.0.2. Self-gravitating Ringlets

N. Borderies et al. 1983b) show that a gravitating ringlet has an equilibrium eccentricity difference $\Delta e^0 = e_{\rm outer} - e_{\rm inner}$ that is stationary. Which means that if a ringlet is in equilibrium, it will precess as rigid body with its streamlines experiencing zero relative motions and with steady Δe over time. Multiplying their expression for the equilibrium Δe^0 by $a/\Delta a$ then provides the ringlet's equilibrium dimensionless eccentricity gradient:

$$e'_{\rm eq} = a\frac{\Delta e^0}{\Delta a} = \frac{21\pi eJ_2}{4H\ q)}\left(\frac{M}{m_r}\right)\left(\frac{R_p}{a}\right)^2\left(\frac{\Delta a}{a}\right)^2 \qquad \text{C1)}$$

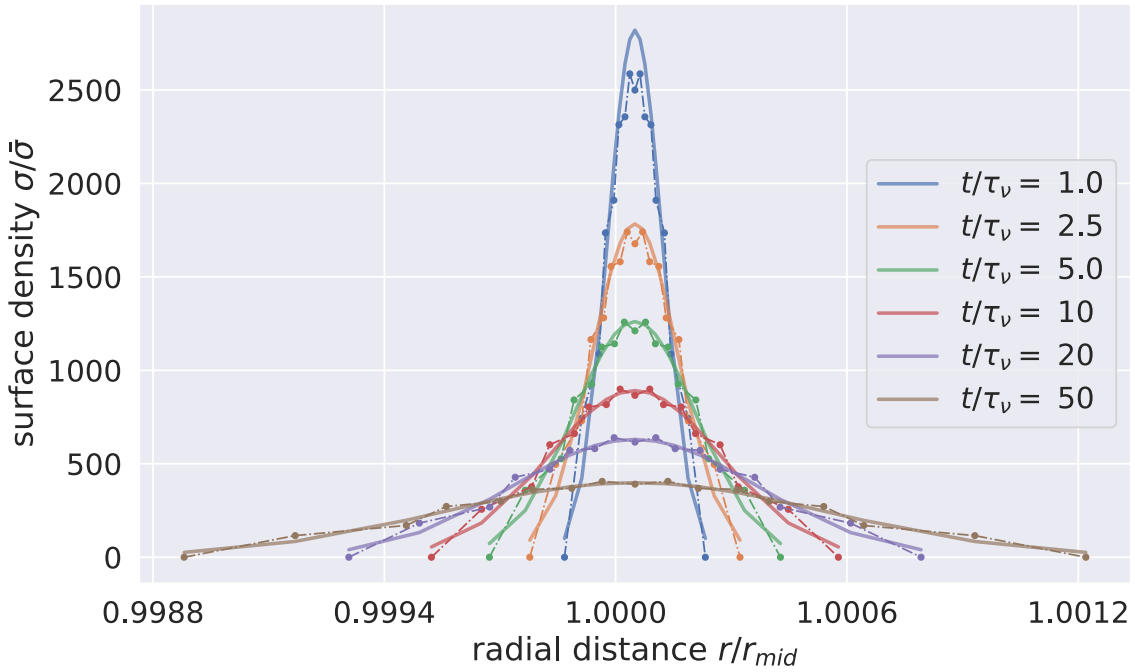

Figure 24. Radial spreading of a initially narrow circular viscous nongravitating ringlet, simulation dashed curves with dots) vs. theory solid curves). The simulated ringlet has the same physical properties as the nominal ringlet: total mass $m_r = 10^{-10}$, initial semimajor axis width $\Delta a_0 = 10^{-4}$, shear viscosity $\nu_s = 10^{-13}$, and bulk viscosity $\nu_b = \nu_s$. However, this simulated ringlet is composed of $N_s = 13$ streamlines instead of two, and all streamlines are initially circular, $e = 0$. nd because a circular ringlet is always axisymmetric, only $N_p = 3$ particles per streamline need be used here. Each colored curve indicates the ringlet's radial surface density profile $\sigma\ r)\ \bar{\sigma}$ vs. radial distance $r/r_{\rm mid}$ at various times t/τ_ν, where τ_ν is the viscous timescale and $r_{\rm mid}$ is the radius of the ringlet's middle. Solid theoretical curves are from Equation 2.13) of J. E. Pringle 1981), where the constant $\bar{\sigma} = m_r\ \pi r_{\rm mid}^2$.

where the nonlinearity parameter $q = |e'|$ since $\tilde{\omega}' =$ for an inviscid ringlet in equilibrium, and the function

$$H\ q) = \frac{1 - \sqrt{1 - q^2}}{q^2\sqrt{1 - q^2}}. \qquad \text{C2)}$$

N. Borderies et al. 1983b) also show that when the ringlet is displaced slightly from equilibrium, e' will librate about the equilibrium point, Equation C1). Which makes it straightforward to iteratively determine a ringlet's equilibrium $e'_{\rm eq}$ numerically via a handful of short epi_int_lite simulations, the results of which are summarized in Figure 25, which compares simulated ringlet equilibria dots) with theory continuous curves) for a variety of inviscid gravitating ringlets. This figure shows that the agreement between the epi_int_lite simulations and theoretical expectations, Equation C1), is overall very good, though modest discrepancies do exist for the higher-mass ringlets whose equilibrium $e'_{\rm eq}$ are small.

nd when a ringlet is displaced slightly from equilibrium, it will librate about the equilibrium point C1) with angular frequency $\Omega_{\rm lib}$ given by Equation 30) of N. Borderies et al. 1983b). So a ringlet's libration period is

$$T_{\rm lib} = \frac{2\pi}{\Omega_{\rm lib}} = \frac{\pi}{H\ q)}\left(\frac{M}{m_r}\right)\left(\frac{\Delta a}{a}\right)^2 T_{\rm orb} \qquad \text{C3)}$$

where $T_{\rm orb}$ is the ringlet's orbital period, which is shown in Figure 26 for the simulated ringlets of Figure 25. This figure compares predicted libration periods dashed curves) versus simulated $T_{\rm lib}$ dotted curves) for the suite of narrow and wide ringlets. The rightmost portions of the blue and green curves show that the higher-mass simulated ringlets' have libration periods $T_{\rm lib}$ that are in excellent agreement with theory, Equation C3). However, significant disagreement exists in the leftmost portions of these curves, which corresponds to the lower-mass narrow and wide ringlets. This disagreement is a consequence of the simulated ringlets' evolution violating a key assumption of the N. Borderies et al. 1983b) derivation: that the ringlet's libration amplitude and its libration frequency $\Omega_{\rm lib}$ are constant during a libration cycle. In all of the simulations reported on in Figure 26, the ringlet's libration amplitude and frequency do vary over time, but those simulations show that their fractional variations $\Delta\ /\ $ and $\Delta\Omega_{\rm lib}/\Omega_{\rm lib}$ are progressively smaller in the higher-mass ringlets. For instance, the three lowest-mass blue and green simulations in Figure 26 have $\Delta\ /\ > 0.5$, while that quantity is significantly smaller for the higher-mass ringlets. From this, we conclude that the lower-mass simulations are exploring parameter space where the theoretical predictions do not apply and that the higher-mass simulations are in excellent agreement with theory.

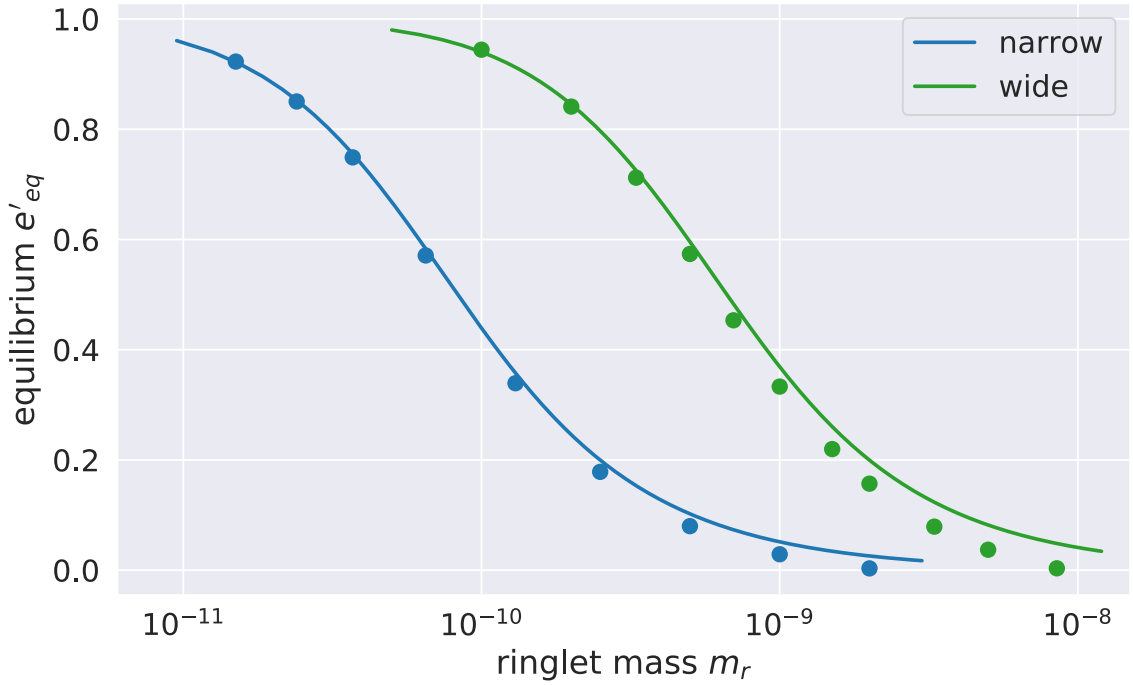

Figure 25. Equilibrium e'_{eq} for two kinds of inviscid $\nu = 0$ gravitating ringlets. The blue curve is for narrower lower-mass ringlets that all have the same semimajor axis width $\Delta a = 5 \times 10^{-4}$, eccentricity $e = 0.0025$, and the indicated range of ringlet masses m_r. The green curve is for wider higher-mass ringlets whose Δa and e are larger by $\times 2$. Dots indicate outcomes from epi_int_lite simulations, while continuous curves are the theoretical predictions from N. Borderies et al. 1983b).

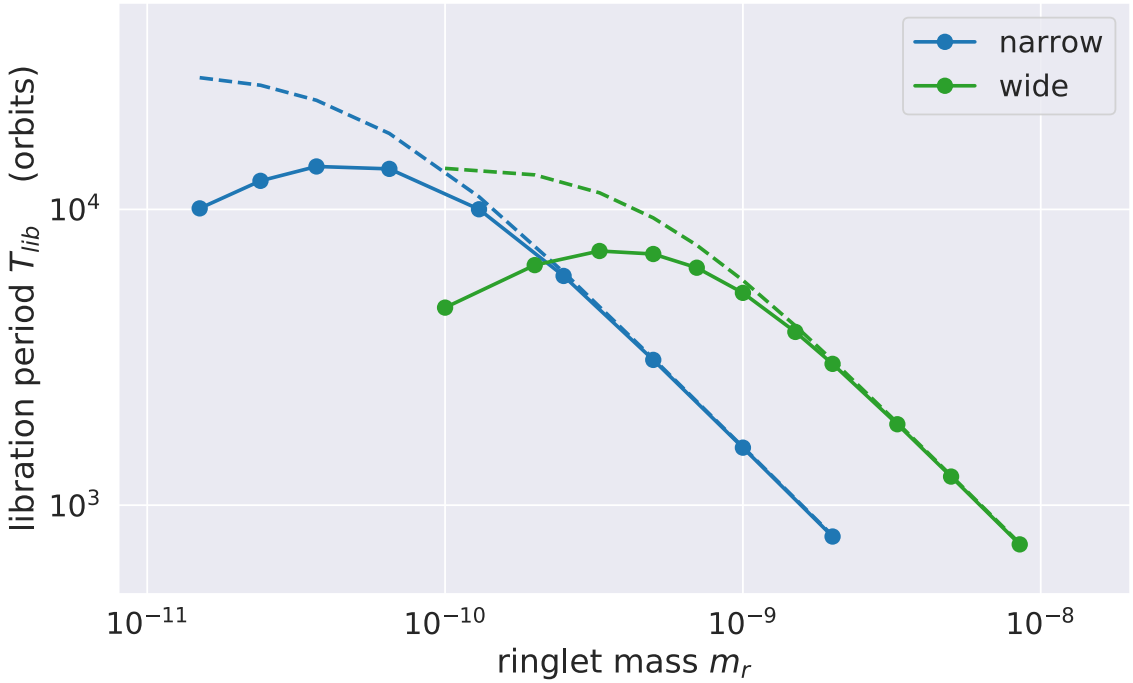

Figure 26. Libration period $T_{\rm lib}$ vs. ringlet mass m_r for the suite of narrow and wide ringlets also simulated in Figure 25. Dotted curves are the simulated outcomes while dashed curves are from Equation C3) derived in N. Borderies et al. 1983b). Note that outcomes for the lower-mass ringlet simulations do disagree with theory, but they are exploring a parameter space where the assumptions utilized in the derivation do not apply.

ppendix D

This examines the viscous evolution of a narrow eccentric nongravitating ringlet that is identical to the nominal ringlet of Section 3.1 but with ringlet self-gravity neglected and $J_2 = 0$.

s the orange curve in Figure 27 shows, the nongravitating ringlet's radial width Δa grows over time due to ringlet viscosity, long after the nominal self-gravitating ringlet blue curve) has settled into the self-confining state by time $t \sim 40\tau_\nu$. This is due to the ringlet's secular gravitational perturbations of itself, which tends to excites the ringlet's outer streamline's eccentricity at the expense of the inner streamline see Figure 3) until the ringlet eccentricity gradient e' blue curve in

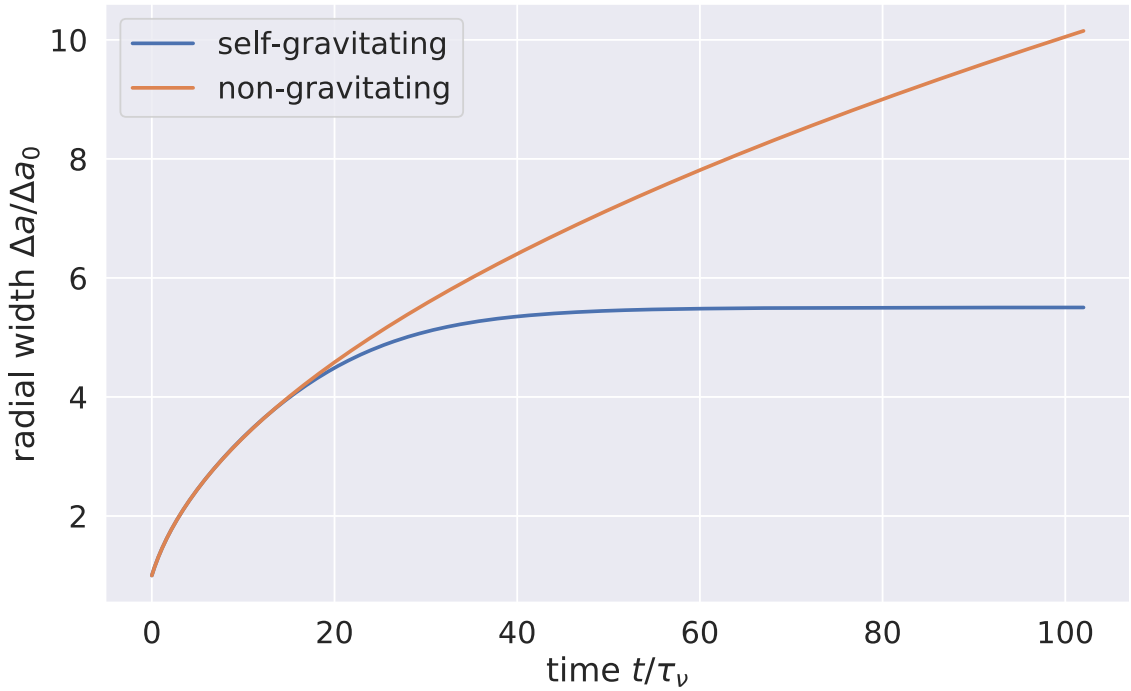

Figure 27. Blue curve is the nominal ringlet's semimajor axis width Δa vs. time t, and this ringlet's radial spreading ceases by time $t \sim 40\tau_\nu$ when its self-gravity has excited the ringlet's eccentricity gradient e' sufficiently; see blue curve in Figure 28. Orange curve shows that the nongravitating ringlet's Δa grows without limit due to the ringlet's much lower eccentricity gradient. Note that planetary oblateness would cause the nongravitating streamlines to precess differentially and eventually cross when $J_2 > 0$, so the nongravitating simulation also sets $J_2 = 0$ to avoid differential precession.

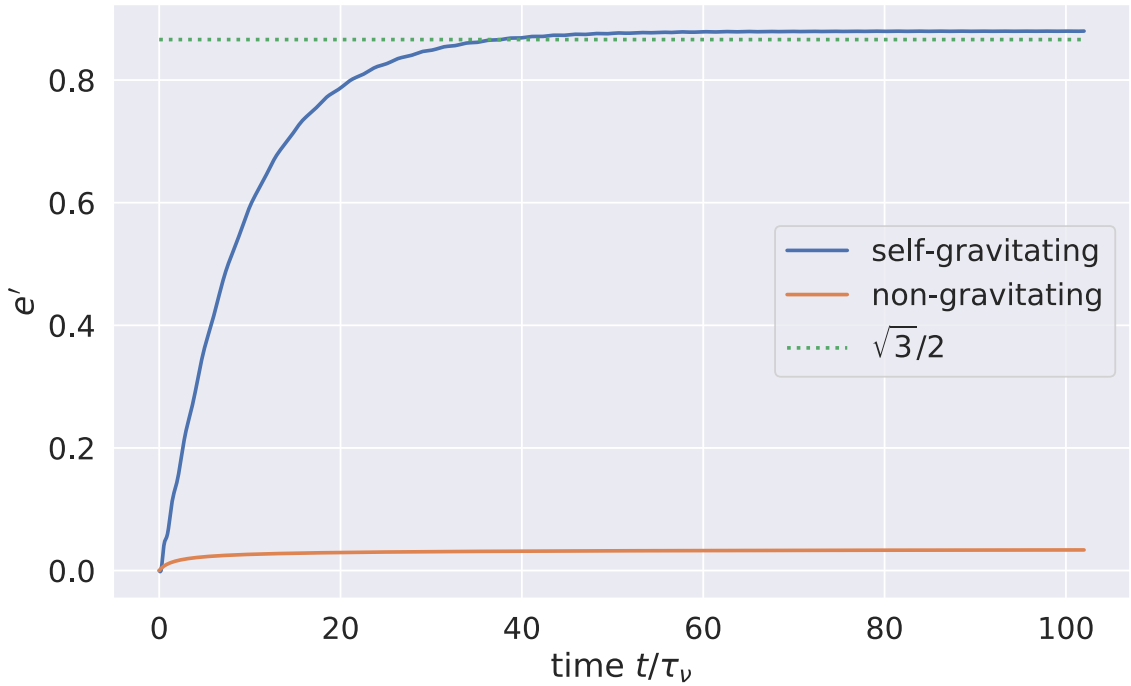

Figure 28. Eccentricity gradient e' vs. time t for self-gravitating nominal ringlet blue curve), and nongravitating ringlet orange).

Figure 28) grows beyond the limit required for complete angular momentum flux reversal that results in the ringlet's radial confinement dotted line). Note that viscosity also excites the nongravitating ringlet's eccentricity gradient some orange curve), but not sufficiently to halt the ringlet's viscous spreading.

ORCID iDs

Yuxi Lucy) Lu https://orcid.org/0000-0003-4769-3273

References

Borderies, N., Goldreich, P., & Tremaine, S. 1982, Natur, 299, 209
Borderies, N., Goldreich, P., & Tremaine, S. 1983a, Icar, 55, 124
Borderies, N., Goldreich, P., & Tremaine, S. 1983b, J, 88, 1560
Borderies, N., Goldreich, P., & Tremaine, S. 1985, Icar, 63, 406
Borderies, N., Goldreich, P., & Tremaine, S. 1986, Icar, 68, 522
Borderies-Rappaport, N., & Longaretti, P.-Y. 1994, Icar, 107, 129
Brouwer, D., & Clemence, G. M. 1961, Methods of Celestial Mechanics New York: cademic)
Chambers, J. E. 1999, MNR S, 304, 793
Charnoz, S., Salmon, J., & Crida, . 2010, Natur, 465, 752
Chiang, E. I., & Goldreich, P. 2000, pJ, 540, 1084
French, R. G., Hedman, M. M., Nicholson, P. D., Longaretti, P.-Y., & McGhee-French, C. . 2024, Icar, 411, 115957
French, R. G., Nicholson, P. D., Hedman, M. M., et al. 2016a, Icar, 279, 62
French, R. G., Nicholson, P. D., McGhee-French, C. ., et al. 2016b, Icar, 274, 131
Goldreich, P., Rappaport, N., & Sicardy, B. 1995, Icar, 118, 414
Goldreich, P., & Tremaine, S. 1979a, J, 84, 1638
Goldreich, P., & Tremaine, S. 1979b, Natur, 277, 97
Goldreich, P., & Tremaine, S. 1981, pJ, 243, 1062
Goldreich, P., & Tremaine, S. 1982, R & , 20, 249
Hahn, J. M. 2009, S/DD Meeting, 40, 6.12
Hahn, J. M., & Spitale, J. N. 2013, pJ, 772, 122
Jones, J. W., Chiang, E., Duchêne, G., Kalas, P., & Esposito, T. M. 2023, pJ, 948, 102
Longaretti, P. Y. 2018, Theory of Narrow Rings and Sharp Edges Cambridge: Cambridge Univ. Press), 225
Matthews, B., Greaves, J., Kennedy, G., et al. 2018, in SP Conf. Ser. 517, Science with a Next Generation Very Large rray, ed. E. Murphy San Francisco, C : SP), 161
Mosqueira, I., & Estrada, P. R. 2002, Icar, 158, 545
Murray, C. D., Chavez, C., Beurle, K., et al. 2005, Natur, 437, 1326
Nicholson, P. D., French, R. G., McGhee-French, C. ., et al. 2014, Icar, 241, 373
Poulet, F., & Sicardy, B. 2001, MNR S, 322, 343
Pringle, J. E. 1981, R & , 19, 137
Rimlinger, T., Hamilton, D., & Hahn, J. M. 2016, S/DD Meeting, 47, 400.02
Shu, F. H. 1984, in I U Coll. 75: Planetary Rings, ed. R. Greenberg & . Brahic Tucson, Z: Univ. rizona Press), 513
Shu, F. H., Yuan, C., & Lissauer, J. J. 1985, pJ, 291, 356
Spitale, J. N., & Hahn, J. M. 2016, Icar, 279, 141
Strubbe, L. E., & Chiang, E. I. 2006, pJ, 648, 652
Tiscareno, M. S., Burns, J. ., Sremčević, M., et al. 2010, pJL, 718, L92
Weiss, J. W., Porco, C. C., & Tiscareno, M. S. 2009, J, 138, 272